ISSN 1349-1113
JAXA-RR-05-007E

JAXA Research and Development Report

Mercury Sodium Atomsphere Spectral Imager (MSASI)

Hiromasa NOZAWA, Ichiro YOSHIKAWA, Shingo KAMEDA,
Hiroaki MISAWA, Shoichi OKANO, Makoto TAGUCHI,
Atsushi YAMAZAKI, Yasumasa KASABA, Koji TAKAMIZAWA,
and Oleg KORABLEV

November 2005

Japan Aerospace Exploration Agency

The Mercury Sodium Atmosphere Spectral Imager (MSASI)

By

Hiromasa NOZAWA[1], Ichiro YOSHIKAWA[2], Shingo KAMEDA[2], Hiroaki MISAWA[3]

Shoichi OKANO[3], Makoto TAGUCHI[4], Atsushi YAMAZAKI[3], Yasumasa KASABA[5]

Koji TAKAMIZAWA[3], and Oleg KORABLEV[6]

Abstract : The Mercury Sodium Atmosphere Spectral Imager (MSASI) on the BepiColombo/Mercury Magnetospheric Orbiter (MMO) is a high-dispersion Fabry-Perot imager. MSASI will address a wealth of fundamental scientific questions pertaining to the Mercury's exosphere. Together, our measurement on the overall scale will provide ample new information on regolith-exosphere-magnetosphere coupling as well as new understanding of the dynamics governing the 'surface-bounded exosphere'. It arises quite clearly from continuous ground-based observations that the regolith of Mercury releases a fraction of its content to Mercury's exosphere. Some processes are identified up to now as leading to this ejection. These processes are associated with different energies of ejection, behavior in different regions of Mercury's surface and eject different types of population from the surface. The responsible processes are (1) Chemical sputtering, (2) Thermal desorption, (3) Photon-stimulated desorption, (4) Ion sputtering, and (5) Micro-meteoroid impact/vaporization. Each candidate seems to be fairly operative, but any cannot completely explain phenomena observed from the Earth. Also, the fate of ejecta from the regolith is still unknown. Some are expected to return to the lithosphere, the other are lost to interplanetary space. Circulation of lithospheric sodium atoms via exosphere-magnetosphere might bring a significant change in the composition of surface layer on Mercury. The MSASI measurements clearly and definitely can identify the release mechanism, how exospheric sodium is born from the regolith, and bring comprehensive picture of global circulation of regolith materials. Also, BepiColombo is the first and unique opportunity to study the formation, circulation, maintenance of this surface-bounded exosphere, which is a different type of terrestrial atmosphere. Below we describe in somewhat more detail the primary scientific objectives of MSASI.

[1] Rikkyo University
[2] University of Tokyo
[3] Tohoku University
[4] National Institute of Polar Research
[5] Institute of Space and Astronautical Science, Japan Aerospace Exploration Agency
[6] Space Research Institute of the Russian Academy of Sciences

1. Introduction

1.1. Introduction of the Hermean exosphere

Mariner 10 made the first measurements of Mercury's atmosphere during the 2 flybys of 1974 and 1975. The ultraviolet spectrometer discovered three constituents; H, He, and O (Broadfoot et al. 1974, 1976). The radio occultation experiments put upper limits on the atmosphere of a few times of 10-12 bar. In addition, ground-based spectroscopic observations revealed the existence of Na (Potter and Morgan 1985, 1987, 1990, 1997a, 1997b; Potter *et al.*, 1999; Sprague *et al.*, 1997, 1998a), K (Potter and Morgan, 1986, Sprague et al., 1990, Sprague, 1992a, 1992b), and Ca (Bida et al., 2000). Table 1.1 gives a summary of the known species and those abundances in Mercury's atmosphere.

Among these species, sodium (Na) is the most populated, and most has been intensively studied since the discovery of Na D-line emissions (589.0 and 589.6 nm) by Potter and Morgan (1985). Continuous efforts further have revealed significant changes of brightness with time and space (Potter and Morgan, 1997; Potter *et al.*, 1999). The characterization of Mercury's sodium distribution should be promoted in a satisfactory way. However, the ground-based observations do not necessarily bring complete understanding of the nature due to inevitable technical and observational limitations, i.e., (i) Mercury is a very close planet to the Sun, (ii) Elevation angle from the horizon is so low that the observation is affected by blurring of the images by atmospheric turbulence, (iii) observational window under twilight condition is very short (about one hour), and so on.

Mean free path in the vicinity of Mercury is ~10^2 km. It means that atoms do not collide with one another, but collide only with the surface of Mercury. Therefore it should be called the surface-bounded exosphere. Atoms in the exosphere have multiple speed distributions that should mainly reflect the release mechanism. According to the initial speed at the time of ejection from the surface, a spatial distribution and its behavior are different. That is, we might know release mechanism based on the spatial distribution of sodium vapor. In such a way, based on 2-D image of Na D-line observed from the ground, some release mechanisms are proposed, e.g., (1) Chemical sputtering, (2) Thermal desorption, (3) Photon-stimulated desorption, (4) Ion sputtering, and (5) Micro-meteoroid impact/vaporization. However, no mechanism can fully explain the observed distribution.

To fully understand the release mechanism of Na atom, the relationship of the exosphere and surface materials, and exosphere dynamics, it is essential that more intensive search by an orbiter should be made. The Mercury Magnetospheric Orbiter (MMO) in the BepiColombo mission studies magnetic field, exosphere, magnetosphere, and inner interplanetary space, and will accommodate instruments mostly dedicated to the study of the magnetic field, waves, and particles in the environment of Mercury (Hayakawa *et al.*, 2004). We propose the Mercury Sodium Atmosphere Spectral Imager (MSASI) as a payload of the MMO spacecraft. Model calculations and laboratory experiments concerning the particle-solid surface interaction will also give us a remarkable progress on understanding of the surface-bounded exosphere.

Table 1.1: Mercury's atmospheric species, column densities, and their emission wavelengths.

Constituent	Column density [cm^{-2}]	Wavelength of airglow [nm]
H	3×10^{9} [a]	121.6
He	3×10^{11} [a]	58.4
O	3×10^{11} [a]	130.4
Na	2×10^{11} [a]	589.0, 589.6
K	1×10^{9} [a]	766.4, 769.9
Ca	1×10^{8} [b]	422.7

[a]Killen and Ip (1999)

[b]Bida *et al.* (2000)

1.2. Description of the Hermean exosphere

1.2.1. Results of observation

1.2.1.1. North-South bright spots

Killen *et al.* (1990) first reported the north-south localized Na emission from their one-dimensional spectroscopic observation. When the slit was oriented to the north-south direction, localized bright spot emissions in the polar region of both hemispheres were identified. Potter and Morgan (1990) confirmed that bright spots of Na emission can be seen on the middle to high latitude in both hemispheres from the two-dimensional spectroscopic observation. In addition, the distribution and intensity of this polar emission can dramatically vary with time, at least, a time scale of one terrestrial day. Some candidates exist concerning this kind of characteristic of bright polar regions as follows. (i) Ion precipitation from the magnetosphere (Potter and Morgan, 1990, 1997a), (ii) sputtering by the solar wind ions (Potter and Morgan 1997b; Potter *et al,* 1999), and (iii) topographic characteristics on the surface (Sprague *et al.*, 1997, 1998). However, it has not been certain yet which process is dominant in Mercury.

1.2.1.2. Dawn-Dusk asymmetry

Sprague *et al.* (1997) reported from their 4 years of observations that average column density of Na atoms in the dawn side is larger than that in the dusk side by a factor of 3 (Table 1.2; after Hunten and Sprague, 1997). Based on their observations, Sprague *et al.* (1998) proposed that ejection of Na atoms from the surface by the sun light (photon-stimulated and thermal desorption) is the cause of the asymmetry. In the dawn side, there are larger amount of Na atoms, which were implanted on cold surface during the night. Most of Na atoms start to eject from the surface at the terminator of the morning. On the contrary in the dusk side, most of Na atoms on the surface have already been exhausted. This is a scenario we have derived from ground-based observations.

Table 1.2: Local time difference of Na abundance (after Hunten and Sprague, 1997).

Early Morning	Mid Morning	Mid Day	Mid Morning	Late Morning
17.2	19	15	6.7	5.2

(Mean low latitude abundances, 10^{10} atoms/cm^{2})

1.2.1.3. Topographic effect

Some researchers propose that the bright spots of Na emissions in the middle to high latitude have relation with the topographic characteristics on the surface (Sprague *et al.*, 1997, 1998). Figure 1.1 gives examples of topographical effect.

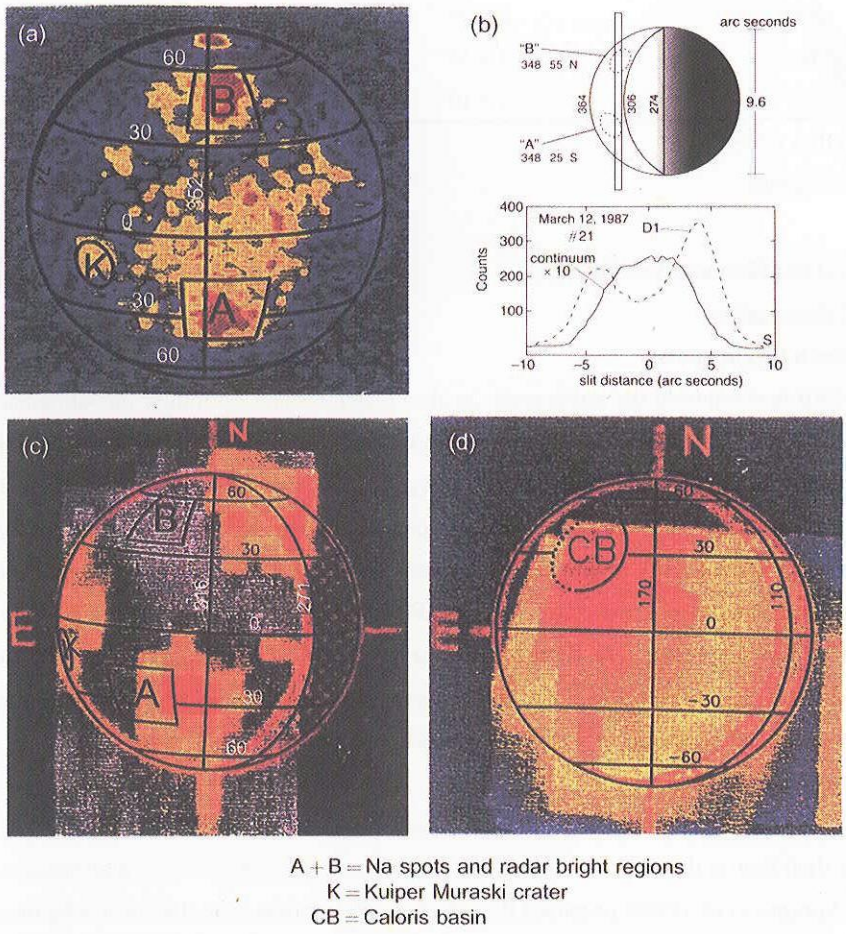

Figure 1.1: (a) Radar image of bright spots (A and B; Slade *et al.*, 1992). (b) Diagram of geometry for slit spectroscopy measurements of Na enhancements over the Radar spots (Sprague *et al.*, 1997). (c) Na enhancements over spot K, A, and unidentified region (Potter and Morgan, 1990). (d) Na enhancement over the Caloris basin Morgan, 1990). After Strom and Sprague (2003).

From the radar observation, Slade *et al.* (1992) discovered the radar bright regions on the high latitude of both hemispheres as shown in Figure 1.1(a). These regions appear bright in radar backscatter because surfaces are rough at the tens of centimeters scale. These regions are expected to be fresh impact craters and be surrounded by fresh blocks of crater ejecta. Bright Na emissions sometimes can be seen over the regions (Sprague *et al.*, 1997).

Another example of the specific topographical region is the Caloris basin in the northern hemisphere. Potter and Morgan (1990) showed Na enhancement over the Caloris basin. This region may be also composed of fresh Na rich rocks.

However it is difficult to conclude that topographic effect really exits. Because both radar bright spots and Caloris basin are located in high latitude, where ion-sputtering from the magnetosphere might be also operative (see section 1.2.2.4).

1.2.1.4. What can we learn from the Moon?

The lunar exosphere exhibits many similarities to that of Mercury. Most obvious is that it has He, Na, and K as three of its constituents (Hodges *et al.*, 1974; Potter and Morgan, 1988; Tyler *et al.*, 1988; Kozloswki *et al.*, 1990). For Na and K, there is less variability and a much smaller abundance than at Mercury (Killen and Ip, 1999). After about a decade of observations of the lunar Na exosphere (Mendillo *et al.*, 1991, 1995, 1999; Sprague *et al.*, 1992, 1998b; Stern *et al.*, 1995; Cremonese and Verani, 1997; Smith *et al.*, 1999; Wilson *et al.*, 2003), some laboratory works studying desorption of Na from Si substrates (Johnson and Baragolia, 1991; Madey *et al.*, 1998; Yakshinskiy and Madey, 1999; Yakshinskiy *et al.*, 2000; Yakshinskiy and Madey, 2001). Theoretical modelings (Flynn and Stern, 1993; Wilson *et al.*, 1999; Wilson *et al.*, 2003) brought us a general picture of what drives the lunar Na exosphere. Basically Na is released from meteoritic and surface materials as atoms and ions. This Na either remains in the atmosphere until it is ionized or swept off the Moon into a "tail" by solar radiation pressure, (see section 1.2.1.) or bounces on the surface where it may stick in cool locations. Then it is released again either thermally as around the sub-solar point where surface temperatures reach 450K (Hale and Hapke, 2002) or by photo-desorption (see section 1.2.2.3). This leads to a two-component thermal distribution and an escaping population (enhanced in the tail). All of these components have been observed, each by different observing techniques.

1.2.1.5. Deformation of sodium exosphere due to solar radiation pressure

The ejected neutral particles are influenced by the solar photons which can push them to anti sunward direction by the solar radiation pressure (Smyth, 1986; Ip, 1990; Smyth and Marconi, 1995; Potter and Morgan, 1987). The effect is highly species dependent and changes by a factor of more than 10 for a sodium atom during the orbital motion of Mercury. This is because the large eccentricity of the Hermean orbit causes a large Doppler shift of deep Fraunhofer absorption at sodium D lines which makes prominent change of radiation pressure acceleration. The radiation pressure plays an important role in the structure of the neutral exosphere; the structure should be dramatically changed according to the orbital position of Mercury. Figure 1.2 is an example of the effect of the solar radiation pressure to the distribution of Na atoms, where the structures are derived from the Monte-Carlo model simulation for sodium atoms released with a constant velocity from the whole Hermean surface. The numbers in the figure indicate the true anomaly angle (TAA), where TAA is defined as the phase angle of Mercury measured from the perihelion position on the orbital plain. On the orbital positions of small radiation pressure (TAA~0°, 180°) the exosphere is confined to the vicinity of Mercury, while, of large radiation pressure (TAA~90°, 270°) the exosphere is stretched to the anti-solar direction forming a tail like structure. In fact, a long tail structure of neutral sodium emission was found at Mercury (Potter *et al.*, 2002; Leblanc and Johnson, 2003). In the model calculation, a photo-ionization process is taken into account as a main loss process whose time-scale varies from 1.6 hours (perihelion) to 3.6 hours (aphelion). The radiation pressure and loss process make the structure of the exosphere asymmetry for approaching and receding phases of Mercury to the sun.

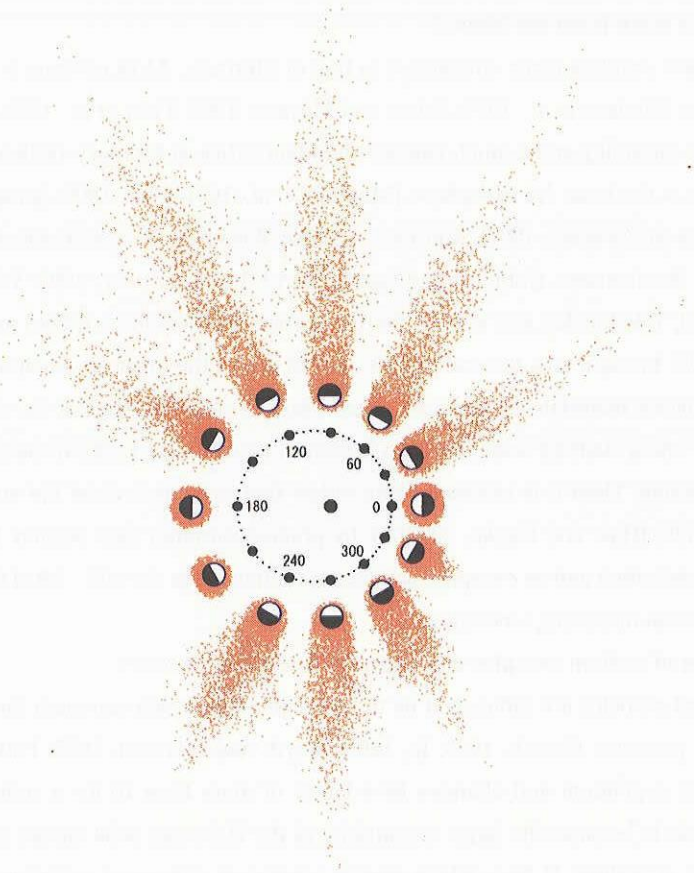

Figure 1.2: Variation of the distribution of sodium atoms with respect to the anomaly angle (TAA) by 30 degrees. In this calculation, particles are uniformly ejected upward from the whole sphere with initial velocities of 3 km/s. The lifetime of sodium atom for photo-ionization varies from 1.6 to 3.6 hours (Takamizawa, 2000).

1.2.2. Release mechanisms of volatile species at the surface

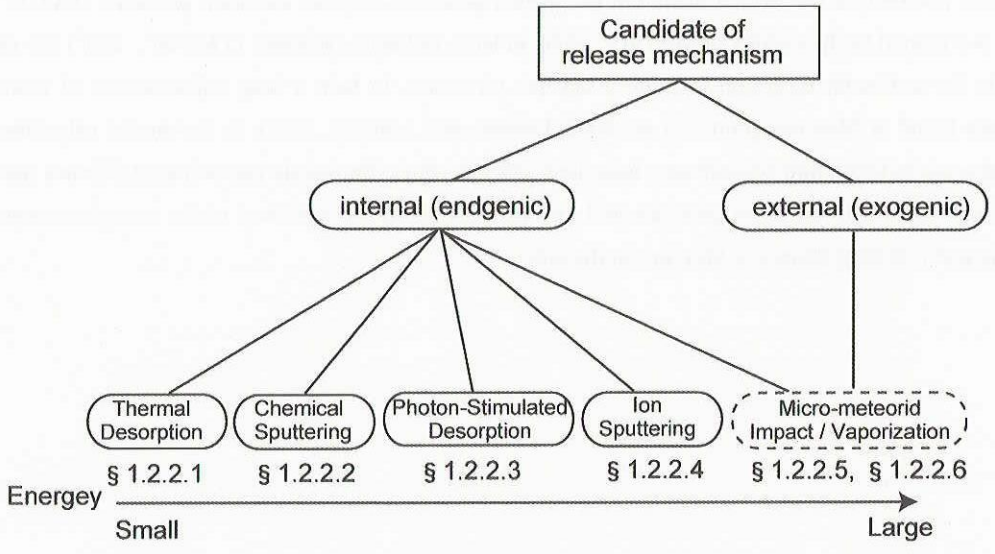

Figure 1.3: Candidates for the release mechanisms.

Up to now, one of the most intensively discussed questions has concerned the relative importance of the different processes of ejection thought to be at the origin of Mercury's exosphere and in particular its sodium component. The problem to identify the sources and sinks for Mercury's exosphere is intrinsically related to this first question. Internal sources of atmosphere must be replenished by regolith turnover, outgassing or diffusion. Recycling of locally formed ions might also be considered an endogenic source. At Mercury, external sources include implantation of impacting meteoroids and comets. The release processes and exogenic source are described in Figure 1.3, and ion recycling is described in section 1.2.3.

1.2.2.1. Thermal Desorption

At Mercury, trace atoms that are bound to or adsorbed on the surface (e.g., Ar at the Moon) can be desorbed thermally (e.g., Hunten and Sprague, 1997, 2002). Whereas thermal desorption refers to ejection of a trace species, like Na at Mercury, sublimation describes ejection of the principal species. The probability per unit time of ejection for thermal desorption is proportional to the surface concentration of a species, cj, to the vibrational frequency on the surface, ν j, and an exponential function of the surface binding energy, Uj:e.g., $dP/dt \approx cj \times \nu j \times \exp(-Uj/kT)$. Thermally desorbed species that are fully accommodated have roughly Maxwellian velocity distributions, typically given as a normalized flux distribution, $f(E, \theta) = [2\cos\theta] \times [E/(kT)^2] \times \exp(-E/kT)$. Applied to Mercury's regolith, this implies that above a surface temperature of 400 K most of the Na atoms will be very quickly thermally desorbed leading to a significant surface's depletion in the early morning of Mercury (Hunten and Sprague, 2002).

This picture is, of course, oversimplified. That is, for any given species, like Na, there are a variety of binding sites (Yakshinskiy *et al.*, 2000). Since the expression above is a probability of ejection, the shallowest binding sites are depleted first so that, in the absence of replenishment, the ejection rate can decrease with time. The time profile of this ejection is greatly modified by the distribution of surface slopes (Hunten and Sprague, 2002). There is another caveat, however, thermal annealing can change the density of binding sites and ion bombardment can produce fresh defects that act as binding sites. In addition, implanted reactive atoms, such as H from the solar wind can occupy vacated sites limiting the availability for a species that is re-adsorbed. Since the lifetime of the grain on the surface is millions of years, in the absence of sources only the most tightly bound intrinsic sodium remains (Killen *et al.*, 2004). However Mercury's surface is constantly bombarded by micrometeorites and a major source is the newly gardened material. That material is not annealed. Therefore the question of the capability and fate of the upper surface reabsorbed impacting exospheric particles remain opened and its answer is fundamental to solve the problem of the volatiles cycling at Mercury.

1.2.2.2. Chemical Sputtering

The incident charged particles and photons can also induce chemical processes called radiolysis and photolysis (Johnson and Quickenden, 1997). The surface is altered down to the depth of penetration by implantation of reactive species (e.g., H, C, O and S) and by bond breaking. In radiolysis and photolysis the surface material can decompose and new, more volatile species can be created which preferentially desorbs changing the stoichiometry (e.g., preferential loss of O_2 from an oxide). The resulting chemical changes in the surface compete with regolith turnover and vapor deposition in determining the surface reflectance.

The chemistry produced by implanted species is often called chemical sputtering (Roth, 1983). The radiolytic processes leading to chemical sputtering consist of several steps: implantation of reactive ions, followed by chemical reactions with target atoms or molecules, and finally, desorption of the reaction products. For cases where the reaction products are volatile, the yield from chemical sputtering may be higher than for other ion-target combinations of similar mass. Sarantos *et al.* (2001) and Kallio and Jahnunen (2003) have shown that solar wind

protons will access the Mercury surface in the polar cusps when conditions of the interplanetary magnetic field are favorable. Potter (1995) suggested that solar protons impacting the surface could yield sodium and water by a chemical sputtering process.

$$2H + Na_2SiO_3 \rightarrow 2Na + SiO_2 + H_2O$$

The reaction of hydrogen atoms with sodium-bearing silicates to yield sodium atoms, water and silicon dioxide is a spontaneous process, thermodynamically favored. Both sodium and water are volatile species that could desorb from the surface. Nash *et al.* (1975) observed strong sodium D-line emission accompanying the sputtering of various rocks by proton bombardment, consistent with the possibility of sodium atom production by chemical sputtering. It should be noted that quantitative laboratory data for the efficiency of chemical sputtering by protons, needed to evaluate the importance of this process on Mercury, is not available so far. The laboratory experiment for this data should made by the BepiColombo mission at the latest.

1.2.2.3. Photon-Stimulated Desorption (PSD)/ Photo-sputtering

Whereas the solar photon flux heats the surface, determining the thermal desorption efficiency, individual photons can excite a bond in the surface (Madey *et al.*, 2002). This can lead to repulsive ejection of an atom, referred to as photon-stimulated desorption (PSD) or photo-sputtering. These terms have been used interchangeably but typically refer to removal of trace species vs. removal of the bulk species (McGrath *et al.*, 1986). Stimulated desorption is less robust than thermal desorption but becomes important when the factor, exp(-Uj/kT), is small. The dominant ejecta are neutrals. Ion ejection requires deeper excitations but, since they are easy to detect, the literature is predominantly on ion desorption. Because ejected ions contribute directly to the local plasma, they might at times be important, but most observed ions are formed by photo-ionization of ejected neutrals.

Adsorbed or intrinsic Na is bound in an ionic form to a silicate (Yakshinskiy *et al.*, 2000). Any Na returning to the surface remains in a physi-sorbed state for a very short time before finding a binding site. An incident photon can excite an electron that attaches to the sodium causing ejection (Yakshinskiy and Madey, 1999). The threshold for desorption from a silicate or an icy surface is only a few eV (Yakshinskiy and Madey, 2001). The desorbed flux, Φ_j for species j, can be written as $\Phi_j \approx \eta_j \sigma_j \Phi$, where Φ_j is the incident photon flux, σ_j is the desorption cross section, and η_j is the number per unit area in the surface. As a first consequence at Mercury, PSD should be maximum at the subsolar point and larger at perihelion than at aphelion. The quantity ($\eta_j \sigma_j$) is also called the yield. The cross section σ_j is the product of an absorption cross section for the photon times the probability of ejection. Whereas gas-phase photo-absorption cross sections for outer shell electrons range from ~10^{-17} to ~10^{-19} cm^2, desorption cross sections can be an order of magnitude or more smaller due to the quenching of the excitations in the solid. Ejected ions can have average energies >> 1eV but ejected neutrals have average energies < 1eV. Stimulated desorption is non-thermal but can have a quasi-thermal component due to the interaction of the exiting atom with other surface atoms. Since planetary surfaces are porous, the ejecta often interact with neighboring grains and, therefore, a thermal distribution with an energetic tail is appropriate. Due to sticking to neighboring grains, the ejecta flux for all processes, including thermal desorption, is reduced by a factor related to the sticking efficiency and the porosity of the surface (Johnson, 1990).

<u>If operative, what image is available?</u> It is known that physical processes and ejection threshold for neutral atoms for the PSD are very similar to those for the electron-stimulated desorption (Killen and Ip, 1999). A laboratory experiment of the electron-stimulated desorption simulating ejection of sodium atoms from the lunar surface showed

that the velocity distribution is quasi-Maxwellian with the peak velocity of about 1km/s (~0.1eV) (Yakshinskiy and Madey, 1999). We have calculated the distribution of the Na exosphere with the Monte-Carlo simulation method for PSD assuming that the ejected sodium atoms follow the Maxwell velocity distribution and the sodium atoms are ejected from the dayside disk (Figure 1.4). We assumed that the sodium surface coverage of the Hermean regolith per unit area and the PSD cross-section are the same as those of the lunar regolith (3×10^{12} atom/cm^2 and 3×10^{-20} cm^2 at $h\nu$ ~ 5eV, respectively, Yakshinskiy and Madey, 1999). The solar photon flux at average heliocentric distance of Mercury is estimated at 1.3×10^{15} photons/cm^2/s at $h\nu$>5eV from the flux at 1AU of 2×10^{14} photons/cm^2/s at $h\nu$ >5eV (Yakshinskiy and Madey, 1999). From these parameters, the PSD flux of sodium from the surface of Mercury is estimated at 3×10^7atoms/cm^2/s and we showed that the estimated column density of the sodium exosphere averaged over the dayside disk is almost comparable to the observed value (~10^{11}atoms/cm^2: 170 kilo-Rayleigh to 3.4 mega-Rayleigh, which depends on g-factors [photons/particle/s]). Our results suggested a possibility that the Hermean exosphere is mainly generated by the PSD process. If it is true, the structure of the sodium exosphere should be basically confined in the vicinity of the surface as shown in Figure 1.4. MSASI will verify the result by clarifying the structure and amount of the exosphere through the quantitative imaging observation.

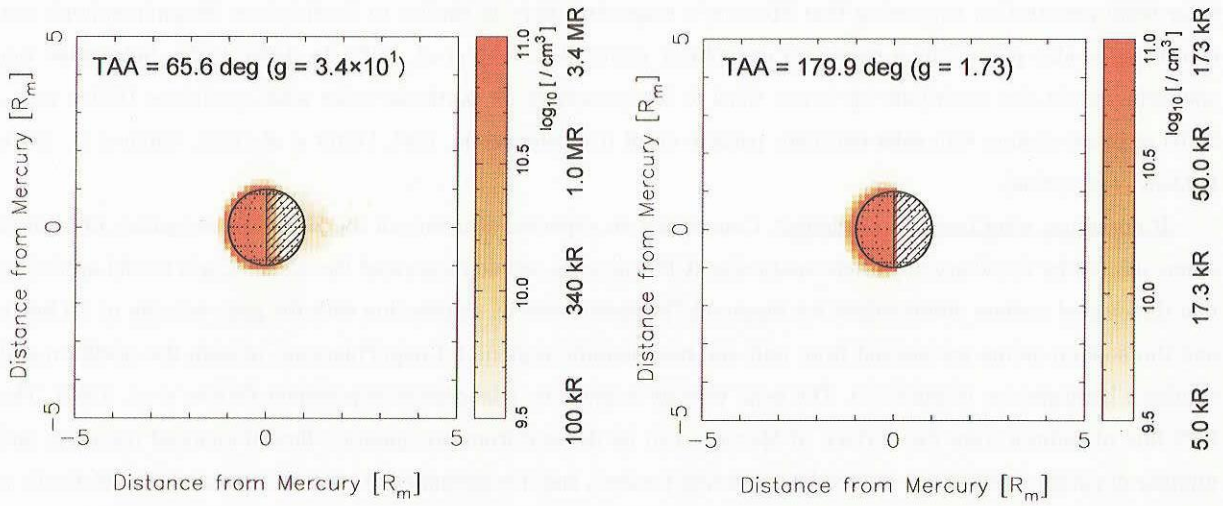

Figure 1.4: Distribution of sodium atoms calculated by the Monte-Carlo model for the photon-stimulated desorption (PSD) process by solar photons. The sodium atoms are assumed to be released from the dayside hemisphere. The true anomaly angles (TAA) are set to 65.6° (left panel) and 179.9° (right panel), where those are the cases of the largest and smallest solar radiation pressure, respectively. Horizontal and vertical axes direct to anti-sunwardand north, respectively. The PSD flux of sodium atom from the surface of Mercury is set to 3.0×10^7 atoms/cm^2/s. The photo-ionization is taken into account as the loss process.

1.2.2.4. Charged-Particle Sputtering (CPS)

Fast ions and electrons from the local plasma can cause desorption and sputtering by exciting the electrons, a process referred to as electronic sputtering. If the density of excitations produced near the surface is low, as is the case for incident electrons and fast protons, then electronic sputtering resembles photo-desorption (Johnson, 1990). However, the fast ions in solar energetic particle events (Leblanc *et al.*, 2003a) can produce high excitation densities that can lead to more efficient ejection. This has not been measured for the species of interest at Mercury, so models have been used. Like for photo-desorption, the ejecta spectrum is not Maxwellian. It has an average energy <1eV, but with a slowly decaying tail. A common fitting form is $f(E)\approx2\times E^x\times U'/(E+U')^{2+x}$, where U' is a fitting parameter which is typically low <0.1eV, E is the energy of the ejecta and $x < 1$.

The incident ions also transfer energy to surface atoms in 'knock-on' collisions (Johnson, 1990). This is the standard sputtering process that leads to non-selective ejection in laboratory studies. Therefore, it is a source of species other than the alkalis or volatiles such as Ar. Knock-on sputtering is often the dominant ejection process in most refractory solids and is most efficient at energies ~0.1-1keV/amu of the incident particles (Johnson, 1990). It has the hardest spectrum with the parameter U' above roughly related to the binding energy of the atom in the material, Uj. It is the most discussed sputtering process. Although there is a large body of data and good computational tools for knock-on sputtering, details for ejection of trace species from planetary materials are sparse. Therefore, one typically assumes stoichiometric ejection, which is valid if the radiation age of the material is large. That is, the sputtering rate is the rate of the erosion of the silicate matrix times the bulk concentration in stationary state (Johnson and Baragiola 1991), or a sputtering yield is often described (the number of atoms ejected per ion incident). That is, in steady state, one uses the atomic sputtering yield of the silicate matrix times the bulk concentration. These yields also need to be corrected for the effect of sticking in the porous regolith.

Typically, ion sputtering has been quoted as a major contributor to Mercury's exosphere in relation to high latitude peak of the sodium exospheric emission (Potter *et al.*, 1999). It is therefore thought to occur in relation with solar wind penetration supposing that Mercury's magnetosphere is similar to Earth's one. Magnetospheric ion sputtering is also potentially a source of exospheric material (Cheng *et al.*, 1987; Ip, 1986, 1987). Solar wind ion sputtering could also contribute up to one third to the exosphere for particular solar wind conditions (Killen *et al.*, 2001) or in association with solar energetic particle event (Goldstein *et al.*, 1981; Potter *et al.*, 1999; Kabin *et al.*, 2000; Leblanc *et al.*, 2003a).

If operative, what image is available? Concerning an expected structure of the Hermean exosphere of sodium atoms ejected by the charged-particle sputtering (CPS) process, we demonstrated the Monte-Carlo model assuming that the ejected sodium atoms follow the Sigmund-Thompson velocity distribution with the peak velocity of 1.5 km/s and the sodium atoms are ejected from only the high latitude regions (~Cusp/Polar-cap) of both the northern and southern hemispheres (Figure 1.5). The peak velocity is given by a laboratory experiment (Wiens *et al.*, 1997). The CPS flux of sodium from the surface of Mercury can be derived from precipitation flux of charged particles, and number of particles which are ejected by sputtering process, and it is estimated at ~6×10^4 atoms/cm^2/s (McGrath *et al.*, 1986). As a result, the estimated column density of the sodium exosphere averaged over the dayside disk is ~4×10^8 atoms/cm^2 (690 Rayleigh to 13 kilo-Rayleigh), which is less than 1% of that generated by the PSD process. In the case of the high radiation pressure condition (TAA=65.6°), average column density of sodium in the night side beyond 3 R_M shows almost the same order as that of the dayside. Our results suggested a possibility that the CPS process is not a main ejection mechanism. However, ground-based observations for the sodium D lines show obvious time variable north-south asymmetries in the middle to high latitude in Mercury and sometimes showed intensity of mega-Rayleigh (Potter and Morgan, 1997b). As the reasons for this discrepancy, following possibilities are considered; 1) the condition of the Hermean regolith is not the same as that of the moon, and (2) total flux of precipitating ions to the planetary surface is much larger than the assumed flux in the model calculation. As for the latter possibility, the rate of intruding solar ions into the Hermean magnetosphere is probably affected largely by the solar wind condition because of the weak magnetic field, then, the amount of ejected atoms should be varied by following the solar wind condition. The answer of this questionable discrepancy between the model estimation and the observational results will be given by BepiColombo; MSASI will evaluate contribution of the ion-sputtering process to the neutral atom ejection by detailed observations for detecting time-variability of the structure with the characteristic time scale of Hermean magnetospheric events which will be identified by simultaneous plasma observations made by MMO, and

condition of the Hermean regolith will be clarified by MPO.

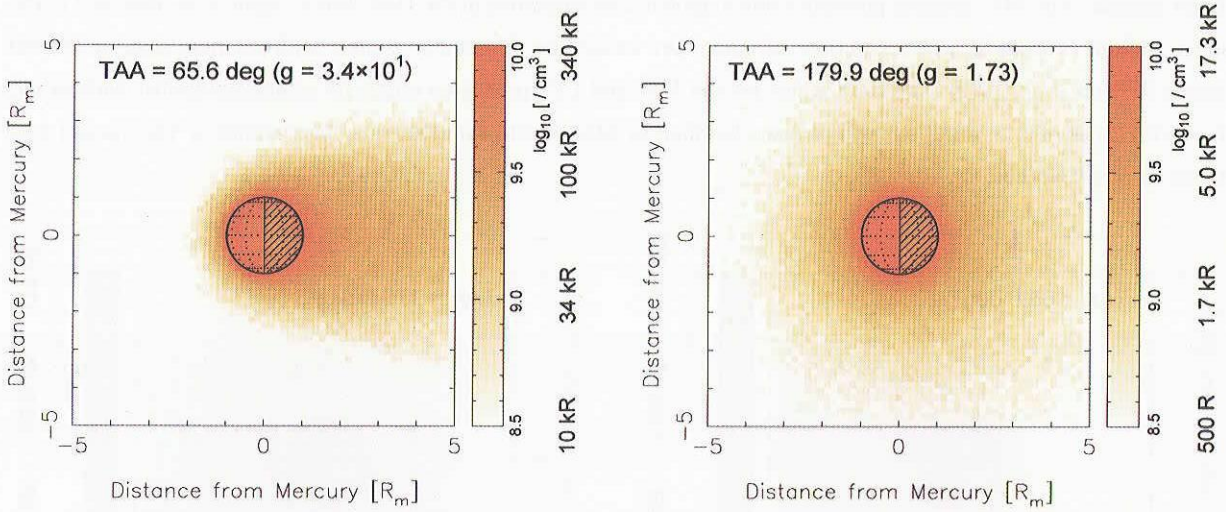

Figure 1.5: Distribution of sodium atoms calculated by the Monte-Carlo model for the charged particle sputtering (CPS) process by the solar wind. The sodium atoms are assumed to be released from only the high latitude regions(Cusp/Polar-cap) of both the northern and southern hemispheres. The CPS flux of sodium from the surface of Mercury is 6×10^4 atoms/cm²/s. A loss process by photo-ionization is included.

1.2.2.5. Meteoroid-Induced Vaporization (MIV)

On impact, meteoroids vaporize grains in Mercury's regolith. Therefore, like knock-on sputtering it is a likely source for species other than the volatiles or semi-volatiles. Meteoroid impact has been shown to be a source of sodium at the Moon (Morgan *et al.*, 1989; Mendillo *et al.*, 1991, 1995, 1999; Wilson *et al.*, 1999, 2003) and is likely important at Mercury (Morgan *et al.*, 1988; Hunten *et al.*, 1988; Cintala, 1992). These impacts also produce the porous regolith, convert surface materials into glasses, and mix the surface exposing fresh material. The vapor is known to coat lunar grains (Hapke, 2001) and can produce an enhancement in the sodium atmosphere during meteor showers (Hunten *et al.*, 1998; Sprague *et al.*, 1998b; Smith *et al.*, 1999). The ejecta exhibit a Maxwellian-like velocity distribution with a temperature between 1500 and 5000 K (O'Keefe and Ahrens, 1977; Sugita *et al.*, 1998) and the amount of material vaporized per impact is of the order of a few times the mass of the impactor (Cintala, 1992). The porous regolith produced by micrometeorite bombardment can severely reduce the sputter flux by shadowing and sticking of ejecta to neighboring grains.

If operative, what image is available? We demonstrated the Monte-Carlo model for the meteoroid-induced vaporization (MIV) process assuming that the ejected sodium atoms follow the Maxwell velocity distribution with the peak velocity of 1.9 km/s (5000K, Sugita *et al.*, 1998) and the sodium atoms are ejected from whole sphere uniformly (Figure 1.6). Morgan *et al.* (1989) estimated the MIV flux of sodium from the surface of Mercury at 2×10^6 atoms/cm²/s at the mean heliocentric distance of Mercury, and we have involved their value in this calculation. The estimated column density of the sodium exosphere averaged over the dayside disk is ~8×10^9atoms/cm² (14 kR to 270 kR), which is nearly 5% of that generated by the PSD process. In the case of the high radiation pressure (TAA = 65.6°), average column density of sodium in the nightside of 3 R_M distance shows somewhat smaller but the same order of magnitude compared with the dayside disk. We suggest a possibility that the MIV process is a minor mechanism particularly for the low altitude exosphere. However, so far the vapor production rate applied also in this model calculation has an ambiguous factor as mentioned in section 1.2.2.6. Quantitative studies on contribution of

each ejection process to the Hermean exosphere will be deferred to detailed investigations of meteoritic materials by BepiColombo. The MIV process possibly leads to global time variations of the Hermean exosphere as observed in the lunar sodium exosphere, where the time variations are caused by the meteor shower with the time scale of several hours (Wilson *et al.*, 1999). The time scales for the MIV and CPS processes might be somewhat similar each other, however, cause of time variations will be also identified by MSASI with simultaneous observations of plasma and dust made by BepiColombo.

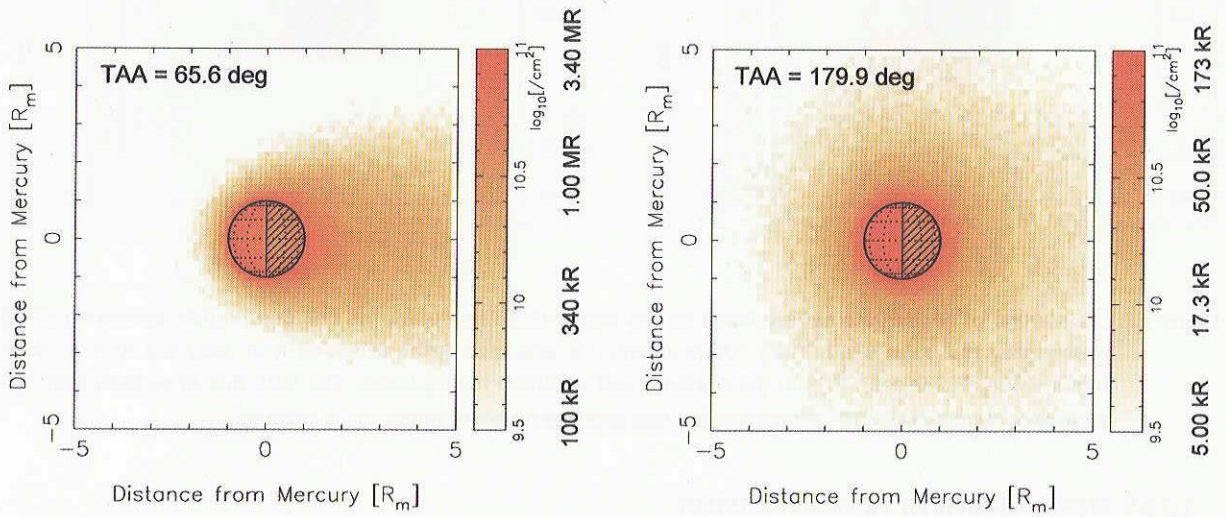

Figure 1.6: Distribution of sodium atoms calculated by the Monte-Carlo model for the Meteoroid-Induced Vaporization (MIV) process. The sodium atoms are assumed to be released from the whole planetary surface. The MIV flux of sodium from the surface of Mercury is set at 2×10^6 atoms/cm^2/s. A loss process by photo-ionization is considered.

1.2.2.6. Meteoritic and Cometary Flux (exogenic source)

Vapor production rates depend not only on the impactor mass flux and velocity, but also on the porosity, density, and the rock types of impactor and target, respectively. Methods of calculating impact vapor yields range from simple impedance matching techniques (Morgan *et al.*, 1988), calculations of phase changes by determining the entropy at each shocked state on a Hugoniot (the locus of possible shocked states) (Cintala, 1992), or using more elaborate hydrodynamic codes (e.g. O'Keefe and Ahrens, 1977; Pierazzo and Melosh, 1999). Although the approaches vary widely in method and complexity, the results agree within a factor of 4 - 5. Additional uncertainties arise because the impactor flux at the orbit of Mercury is not well known. However, a factor of 5 difference is large enough that conclusions concerning the fraction of the atmosphere supplied by impact vaporization range from about 10-20% (Killen *et al.*, 2001) to near 100% (Morgan *et al.*, 1988). Although variations in the impact-generated lunar atmosphere may arise due to meteor showers (Barbieri *et al.*, 2001; Hunten *et al.*, 1998; Smith *et al.*, 1999; Verani *et al.*, 2001), it is less likely that Mercury will be impacted by periodic meteor showers since the aphelion is greater than 0.46 AU.

The density of meteoritic material in space at Earth orbit has been measured by the Long Duration Exposure Facility to be 3×10^{-16} g cm^{-3} (Love and Brownlee, 1993) and can be scaled to orbital distance, R_{orb}, as $R_{orb}^{-1.3}$ (Morgan *et al.*, 1988; Cintala, 1992). The mass density measured by the Long Duration Exposure Facility includes the mass in the range 10^{-9} to 10^{-4} g; an equal amount is assumed to be in the 1 cm to 10 km size range (Ceplecha, 1992).

Differences between various vaporization estimates (Cintala, 1992) are explained for the most part by choice of mass influx, porosity, and impactor and regolith composition and density. Although increased porosity will increase the vapor production in theory, a very dense impactor on a very porous target may simply bury itself too deeply for the

vapor to easily escape. The meteoritic flux at the heliocentric distance of Mercury depends also from the particle size as they follow a different dynamical evolution. Meteoritic size smaller than about 1 mm regards particles with a dynamical evolution dominated by the Poynting-Robertson effect and the estimates of the flux should be good and not easily improved. While particles having a larger size follow a completely different dynamical evolution, for instance most of them, arriving on the terrestrial planets, come from two important resonances located in the asteroid main belt (the resonance 3:1 with Jupiter and a secular resonance with Saturn). At the moment the flux estimates are quite rough at the Mercury distance. Thus, while the calculations are indicative that impact processes are important at Mercury, and probably produce a factor of 5 more vapor at Mercury than at the Moon, much uncertainty exists as to the relative importance of this process with respect to other source processes.

The knowledge of density, size, velocity, and composition of meteoroids and comets is necessary to know the contribution of exogenic materials, like sodium in the Earth's upper atmosphere, to Mercury's exosphere.

1.2.3. The fate of sodium after the release

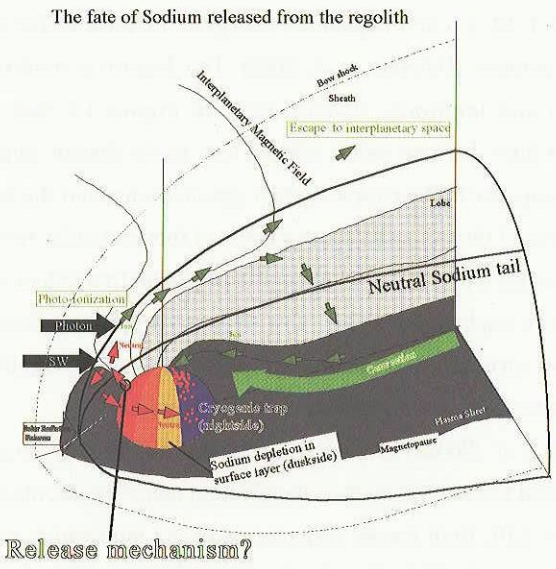

Figure 1.7: Schematic description of Na circulation around Mercury.

The fate of sodium after the release is also an interesting topic. There is no observation to clarify sodium circulation around Mercury. Figure 1.7 shows the schematic description of our current understanding of global sodium circulation.

It arises quite clearly from the previous sections that the regolith of Mercury releases a fraction of its content to Mercury's exosphere. The different processes identified up to now as leading to this ejection were described before.

The neutral particles are ejected from Mercury's surface with an energy around 1 eV, the most energetic process of ejection being ion sputtering (up to few eVs) and the less energetic, thermal desorption with less than 0.1 eV at Mercury's subsolar perihelion when the surface temperature reaches 700 K (Chase *et al.*, 1976). After ejection, most of the neutral particles because they have energy less than the escape energy (0.1 eV/amu) will follow a ballistic trajectory and re-impact the surface where they will be reabsorbed. Such particles are then re-ejected until they meet regions where the ejection probability decreases significantly (Hunten and Sprague, 1997). Typically such regions correspond to Mercury's nightside where most of the ejection processes do not work and where the cold surface act as a cryogenic trap.

The ejected neutral particles are also influenced by the solar photons which can ionize part of these neutral particles. Otherwise they can push neutral sodium atoms in the anti-sunward direction by the solar radiation pressure (Smyth, 1986; Ip, 1990; Smyth and Marconi, 1995; Potter and Morgan, 1987), and forms a neutral tail (Potter *et al.*, 2002). Both effects are changing from perihelion to aphelion of Mercury and are highly species dependent. The ionization of the neutral is a sink for the neutral exosphere and as a source for the magnetosphere. The radiation pressure plays an important role for the structure of the neutral exosphere; the structure should be changed according to the orbital position of Mercury (Smyth and Merconi, 1995).

Both spatial and temporal scales, the characteristic scales of field variations are much smaller at Mercury than at Earth. A first straightforward consequence of small spatial scales at Mercury is the centrifugal acceleration that affects particles during transport. Regardless of their origin (solar wind or planetary exosphere), ions traveling from high to low latitudes are subjected to enhanced outward oriented parallel acceleration due to the large curvature of the $\mathbf{E}\times\mathbf{B}$ drift paths. This leads to populations in the magnetospheric lobes that are substantially more energetic (typically, a few hundreds of eVs) than at Earth (Delcourt *et al.*, 2002).

Figure 1.8 displays intense ($\sim 10^6$ $s^{-1}.cm^{-2}$) impacts of energetic (several keVs) ions within two latitudinal bands that extend over 10°-20° at mid-latitudes (Delcourt *et al.*, 2003). This feature is confirmed by hybrid simulations of ion circulation at Mercury (Kallio and Janhunen, 2003b). Note in Figure 1.8 that the poleward boundary of the precipitation bands follows from finite Larmor radius effects, ions in the distant (typically, beyond 3 planetary radii) tail intercepting the dusk magnetopause in the course of their gyromotion about the small B_Z component.

Leblanc *et al.* (2003b) illustrated the potential consequence of this particular recycling of the Na^+ ions within the magnetosphere. These authors using typical solar wind conditions found that enhancement in the Na emissions could be correlated to these bands of re-implantation. They also suggested that any change in the solar wind conditions could change the magnetospheric structure (Luhmann *et al.*, 1998) and induce significant changes in the recycling of magnetospheric ions inducing correlated variation in the neutral exosphere.

On the other hand, Misawa *et al.* (2002a) evaluated the amount of the recycling sodium ions for several sodium ejection processes. They calculated the neutral sodium distribution using the Monte-Carlo model simulation (see also Takamizawa *et al.*, 2000, Figure 1.9), then traced trajectories of Na ions which were mainly made by the photo-ionization process (Killen and Ip, 1999). The photon-stimulated desorption process supplies about 25% of ejected sodium atoms to the Hermean magnetosphere as the ions and nearly the half of them return to Mercury (Killen *et al.*, 2004). The processes of ion-sputtering and meteoroid-induced vaporization supply about 15% of ejected sodium atoms to the magnetosphere and nearly the half of them returns to Mercury. The rate of the returning ions is not so large, however, the re-implantation of the magnetospheric ion on the surface occurs mainly at particular regions (Leblanc *et al.*, 2003b; Killen *et al.*, 2004; Massetti *et al.*, 2003) and could also lead to significant variation of the volatile surface concentration (Ip, 1986; Sprague, 1990). This recycling process might explain the dawn-dusk asymmetry and latitudinal dependence of neutral sodium distribution. As a consequence, this explanation leads to consider a finite reservoir for Mercury's exosphere, therefore that release processes can compete between each other to eject particles into the exosphere (they do not act on an infinite reservoir) and that in certain regions of the surface a significant depletion can occur. Unfortunately we know very few on the different sources and sinks at Mercury and up to the forthcoming missions to Mercury little information can be expected from ground based observations.

The day to night sides migration of the Na atoms generates a non uniform surface density of the Na atoms on the nightside. The surface density is larger at high latitudes than at equatorial latitudes on the nightside (Leblanc and

Johnson, 2003) because high latitude regions reach temperature above 400 K few Earth days later than equatorial region. As a consequence it produces a larger release of Na atoms at high latitudes than at equatorial latitudes when these surfaces reach the hot dayside (Hunten and Sprague, 2002; Leblanc and Johnson, 2003).

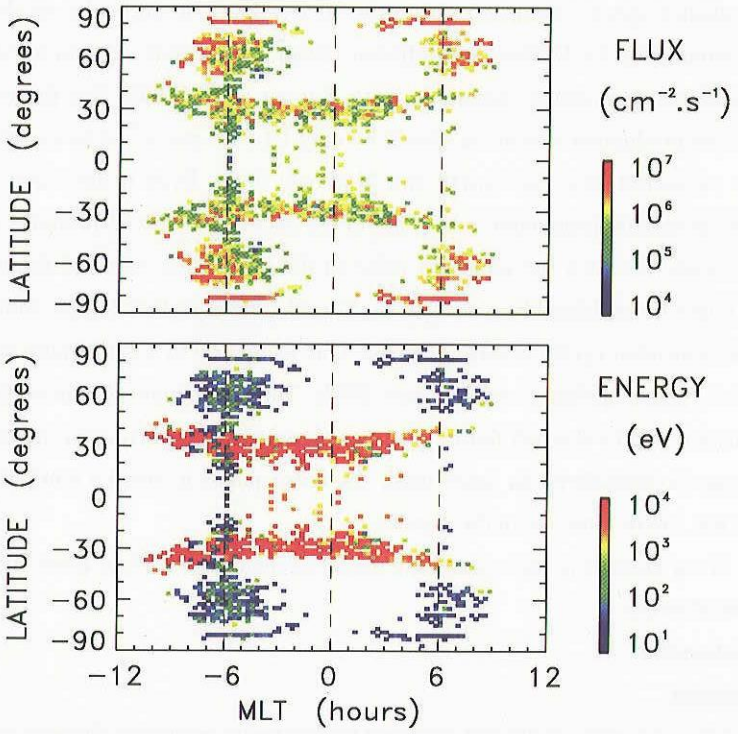

Figure 1.8: Color-coded flux (top) and average energy (bottom) of precipitating sodium ions as a function of magnetic local time and latitude (Delcourt *et al.*, 2003).

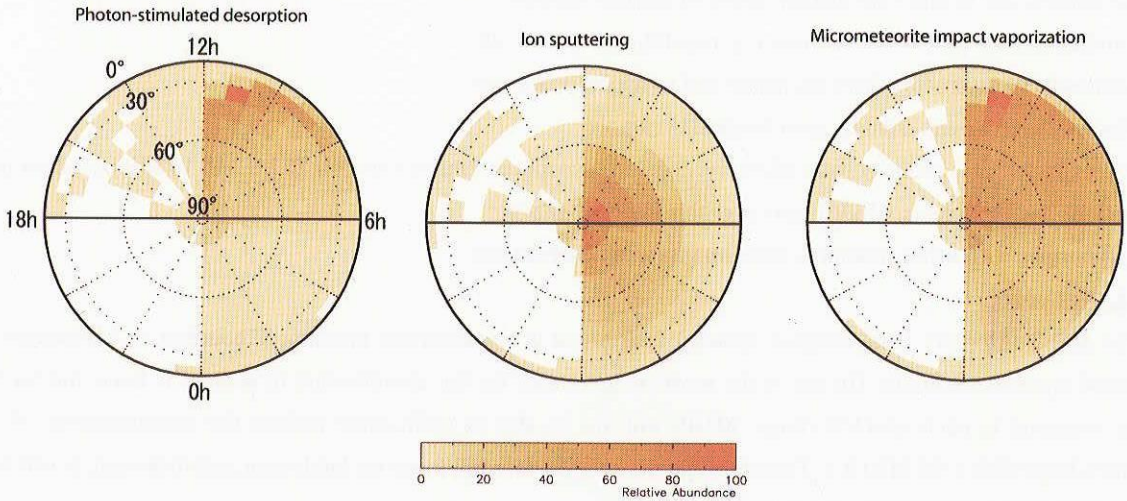

Figure 1.9: Distribution of the return sodium ions for each ejection process in the northern hemisphere with respect to latitude and local time, which are divided into every 10 degrees and 40 minutes. (a) Photon-stimulated desorption, (b) Ion sputtering and (c) Meteorite induced vaporization. Normalized amount of sodium ions are shown in these panels. Normalization was carried out in each panel (Misawa *et al.*, 2002a).

Leblanc and Johnson (2003) showed the result of the strong depletion of Na atoms on the dayside in Mercury surface and the result of the migration of these Na ejected from the dayside (mainly from the morning side of the planet). An increase of the Na density was verified in the very early morning because of the reabsorption by the cold surface. Moreover a maximum in this density is produced at high latitudes.

The amount of volatiles species adsorbed within the surface layer, in particular on the night side, is basically unconstrained. From simulations by Leblanc and Johnson (2003), the dayside exosphere contains 100 to 1000 times less sodium than the nightside regolith. Assuming, with Hunten *et al.* (1988), that the erosion rate of Mercury's regolith is 0.19 Å /yr, the production rate of Na should be only 1.1 (10^4 cm^{-2} s^{-1}, to be compared to the value of a few 10^7 cm^{-2} s^{-1} currently estimated (see e.g. Smyth and Marconi, 1995). Even if the main source of Na is infalling meteoritic matter, the net sodium production rate is not in excess of 10^5 cm^{-2} s^{-1} (Hunten *et al.*, 1988). The difference by 2-3 orders of magnitude between the expected value of the production rate and the value required to explain sodium observations might be explained by a net day/night exchange of sodium atoms, which would undergo a great number of adsorption-desorption cycles before escaping. This factor 100 to 1000 is quite similar to the result of the simulation as mentioned above (Leblanc and Johnson, 2003). The day-to-night flux of sodium atoms is obtained by multiplying the production rate by the half duration of one Mercury day (1 terrestrial month), and is of the order of 10^{14} cm^{-2}. This value may be considered an upper limit, and corresponds to about a tenth of a monolayer, which may be present in the first few μm or tens μm of the regolith.

The main object of our study is to understand the global circulation of sodium (after the release), influencing the surface composition of Mercury.

1.3. Proposed investigation

1.3.1 General objectives

The general scientific objectives of MSASI, oriented toward better understanding the coupled surface-exosphere-magnetosphere system described in previous parts, may be summarized as follows:

- Spatial distribution of sodium exosphere and its variation.
- Dynamics: day to night circulation, active to inactive regions.
- Surface release processes, sources: e.g. regolith, meteorites, etc.
- Atmosphere/magnetosphere exchange and transport processes.
- Escape, source/sink balance, geochemical cycles.

The expected line intensity from Mercury's sodium exosphere ranges between 20 kR and 10 MR based on past observations and modelings. MSASI can cover this intensity range.

1.4. Synergies with other missions, instruments and observations

1.4.1. Messenger

The MDIS (Mercury Dual Imaging System) instrument is a counterpart instrument boarded on Messenger. A fairly good spectral resolution (10 nm at the most) is not aimed for the identification of sodium D lines, but for the surface mapping in each spectral range. MDIS will not be able to sufficiently reduce the contamination of the Mercury's bight disk (~50 MR/Å). Therefore the exospheric data will focus on Limb-scan, not disk-scan. It will be a strong constraint to understand exospheric nature.

Although MDIS addresses the same scientific objective as MSASI, advantages of our MMO instrument deserve to be mentioned.

- Good spectral resolution can clearly identify the sodium D2 line.
- Spinning spacecraft (MMO) can provide the good platform to command wide perspective over the Mercury's

sodium exosphere.

1.4.2. Mercury Planetary Orbiter (MPO)

According to the Mercury Planetary Orbiter (MPO) Payload Study Document, ultraviolet spectrometer (UVS) will probably detect a large number of species, although some of them are already known. The existence of rarefactory element and/or its abundance in the exosphere are important clue to study the exospheric origin. If rarefactory gases like Ca and Fe are rich in the vicinity of Mercury, it means that the source process of gas element is companied with large energy such as meteoroid impact. On the other hand, if volatiles (Na, K) are rich, that means a smaller energy process is dominant. Therefore, the compositional measurement by UVS is also important.

However 2-D images, which are available from the MMO (MSASI) investigation have advantage on study the circulation and sink of atoms in the large field, i.e., surface, exosphere, and magnetosphere, because such study needs a wide-field-of-view observation.

Second, there will be a strong synergy with a potential limb imager of sodium emission. Although MSASI on MMO will allow probing whole the exosphere, additional information will be derived from limb observations. The better spatial resolution (a few km) and longer exposure time will be achieved. However, spatial coverage of limb camera highly depends on an MPO trajectory and also only a highly bright region can be observed (Because limb camera detects weaker sodium emission line at 330 nm, not D-lines, according to the MPO Payload Study Document). Nonetheless, the combination of limb observation of Na from MPO and global vertical profile obtained by MSASI at different latitudes and longitudes will provide a complete picture of the exospheric sodium structure and dynamics.

There is an interesting synergy with the MPO X-ray and Gamma-ray measurements of the chemical composition of the near subsurface material. It will be possible tentatively to compare Na concentration on surface and its circulation in the exosphere, which are expected to be closely inter-related in an average over time.

1.4.3. Ground-based observations

In preparation for the arrival of BepiColombo at Mercury, there should be a comprehensive set of ground-based observations to characterise morphology patterns and issues, thus helping to focus science strategies and priorities once the spacecraft starts its *in situ* program. During the data-collection part of the mission, the intensity of the observation program should be increased. Following the mission, there must be a synthesis of the *in situ* observations and the ground-based data to arrive at a more complete understanding of Mercury's exosphere.

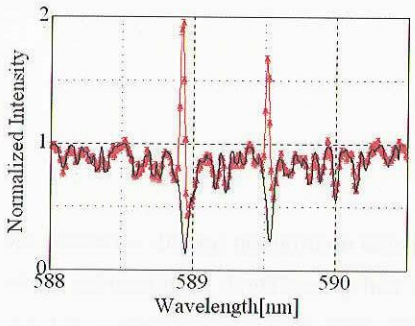

Figure 1.10: The spectrum around the sodium D lines observed for Mercury on April 22, 2003 (red) andthe calculated spectrum (black).

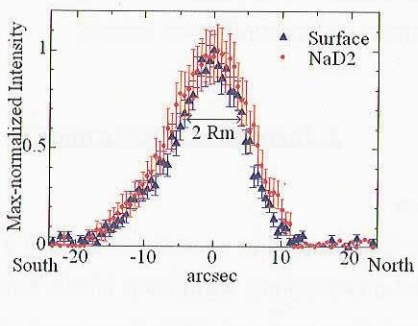

Figure 1.11: North-South distributions of the intensity of Na D_2 emission (red) and the surface reflection (blue) on April 22, 2003.

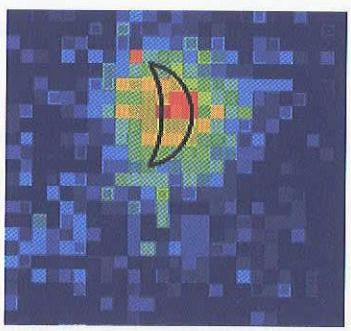

Figure 1.12: 2-D image of Na D_2 emission obtained with Fabry -Perot interferometer on June 6, 2003.

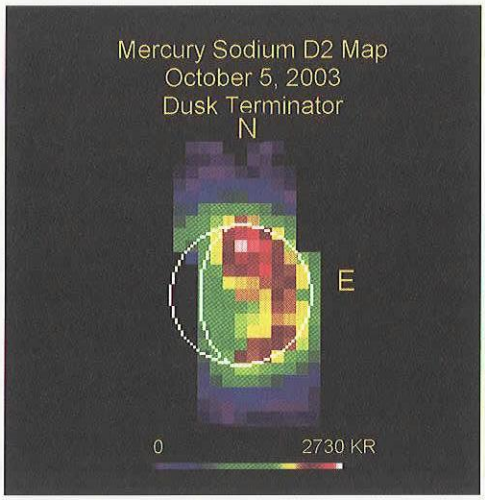

Figure 1.13: An example of the sodium images obtained with tip-tilt stabilization (Potter *et al.*, 2004).

We have just started the observation program for Mercury's sodium exosphere at the Iitate Observatory, Japan in 2003. We mainly use a Fabry-Perot Interferometer as a 2-D imaging system, which achieves a high spectral resolution of 0.01 nm. Figure 1.10 shows one of the observed spectra of Mercury. The intensity of NaD2 emission was approximately 6 MR and the corresponding column density was estimated to be $3.0 \pm 0.5 \times 10^{11}$ atom/cm^2 in 2003. Figures 1.11 and 1.12 show the spatial distribution of sodium exosphere. Unexpectedly, neither North-South bright spot nor rapid change (~1 terrestrial day) could be seen during this period. We have continued to observe sodium emissions from Mercury's exosphere for the long-term period (1-2 weeks) every elongation. During the orbital phase of the BepiColombo mission, attention and request for this program should increase.

A problem with current ground-based observations is the lack of good spatial resolution caused by blurring of the images by terrestrial atmosphere. Our U.S. colleague has just improved this problem. Potter *et al.* (2004) used a high speed tip-tilt image stabilization system to provide improved spatial resolution for the sodium distribution, and are developing true adaptive optics stabilization for Mercury images. An example of the sodium images obtained with tip-tilt stabilization is shown in Figure 1.13. It is expected that by the time of BepiColombo arrival at Mercury, much better sodium and potassium images will be available from ground-based observations, and will enable a very good synthesis of the orbital observations with ground-based images.

2. Instrument Performance

2.1. Main measurement objectives

Mercury's sodium exosphere will be studied in a satisfactory way if a spatial distribution and its variations are made clear. From the ground-based observations, significant North/South and Dawn/Dusk asymmetries of the sodium exosphere have been reported (Sprague *et al.*, 1997; Potter *et al.*, 1999). Such nature is mysterious, but also very important clue to understand the release mechanisms of sodium (discussed in previous sections).

Five main categories of measurement objectives can be identified:

1- To image sodium exosphere with a spatial resolution of better than 1/64 R_M. This resolution is good enough to find sodium rich spots on the surface, e.g. radar bright spots, Caloris basin, etc.

2- To measure local and temporal variations of the sodium exosphere (time scale: less than a few hours), at specific times (short; substorm, middle; North/South asymmetry, long; distance from Sun) and regions of interest (Caloris Basin, polar regions, etc.). Acquisition of full disk image a minute is a baseline.

3- To identify release mechanisms which are stimulated by incoming materials such as solar photons, solar wind ions and micro-meteoroids.

4- To understand global circulation of sodium among surface-exosphere-magnetosphere. (The X- and Gamma-ray investigations of MPO are also important).

5- To find an ion source region for the magnetosphere. (Simultaneous observations of plasma and dust are necessary).

2.2 Coverage and Sampling

Figure 2.1 shows the orbit of the MMO spacecraft on the meridional plane. The orbit is polar and highly elliptic; its major axis lies close to the equatorial plane to permit a global exploration of the magnetosphere from an altitude of 400 km up to nearly 12,000 km during 9.3 h orbital period. Mercury has an apparent diameter of 30° near the apoherm. MMO is spinning spacecraft. The spin axis is nearly perpendicular to the Mercury orbital plane. The spin period is 4 sec. The current baseline of the conceptual design of the MMO spacecraft is described by Yamakawa *et al.* (2004). Combining a spinning motion of the MMO spacecraft and usage of the one-degree-of freedom scanning mirror, we can obtain a two-dimensional image over the Mercury's disk, exosphere and magnetosphere. A schematic picture of the observation is shown in Figure 2.2.

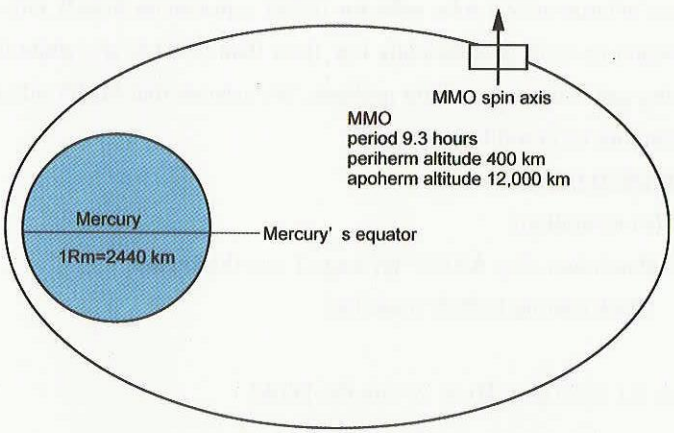

Figure 2.1: A trajectory of the MMO spacecraft

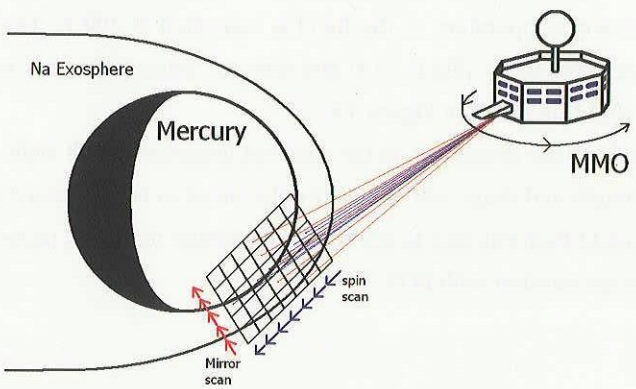

Figure 2.2: Method of the MSASI observations.

3. Technical Description and Design

3.1. Design Requirements

- The requirement for line detection of sodium D2 emission (589.1583 nm in space) is a signal-to-noise (SN) ratio of 10 for average line intensity (100 k - 10 MR).
- Sensitivity to Sodium D2 line is as weak as 20 kR (depending on the stray light background). Maximum intensity is expected by 10 MR.
- A spectral resolution of 0.007 nm is necessary.
- A spatial resolution of at least the same scale as scale height of sodium, i.e. 40 km. When observing from apoherm, this translates into a spatial resolution better than 0.17°.

3.2. Design description

3.2.1. General description

A general layout of MSASI and subsystems are shown in Figure 3.1. The instrument consists of four subsystems, MSASI-H (Hood), MSASI-G (Gearing system and front optics), MSASI-M (Main body of instrument) and MSASI-E (Electronics and detector). Figure 3.2 shows optical layout of MSASI. An installation of MSASI on the MMO spacecraft is shown in Figure 3.3. A field of view of MSASI is below the horizontal plane.

To reduce stray lights, we require that

(1) Any extensions and object are behind Plane-A shown as a red-dashed line in Figure 3.3,

(2) To avoid solar random reflection on the side panel beneath the hood (Area-B in Figure 3.3), it is highly required that one piece of large optical solar reflector (OSR) is placed on Area-B. Our experimental result shows that the random reflection on OSR is sufficiently low (less than 0.003 %/sr), while the edge of OSR plane will cause random scattering and bring a stray light problem. We assume that MMO side panel is covered with OSR, whose size is a few centimetres in width and height.

3.2.2. Subsystem 1 : MSASI-H (Hood)

Lead institution: ISAS [PI institution]

- Substrate material: Aluminium alloy A5052P (average 1 mm thickness)
- Inner coating: Black coating JEF302 (baseline)
- Outside: OSR
- Size: 150 mm (L) × 50 mm (H) × 72 mm (V) [TBR]

The temperature of the hood will become much higher than inside of the spacecraft. According to a thermal model calculation, the maximum temperature of the hood is estimated at 400 K. Therefore, MSASI-H should be thermally isolated from other subsystems (Figure 3.4) and directly connected with screws to the side panel of the spacecraft. Installation of MSASI-H is shown in Figure 3.5.

Length and shape of the hood are dependent on the apparent diameter and tilt angle of MMO relative to the Sun. After the AO selection, the length and shape will be finally determined to be minimized on the condition that (1) the hood prevents the direct sunlight from entering to the entrance aperture during all phase of spin motion of the MMO spacecraft, (2) the hood does not interfere with FOV.

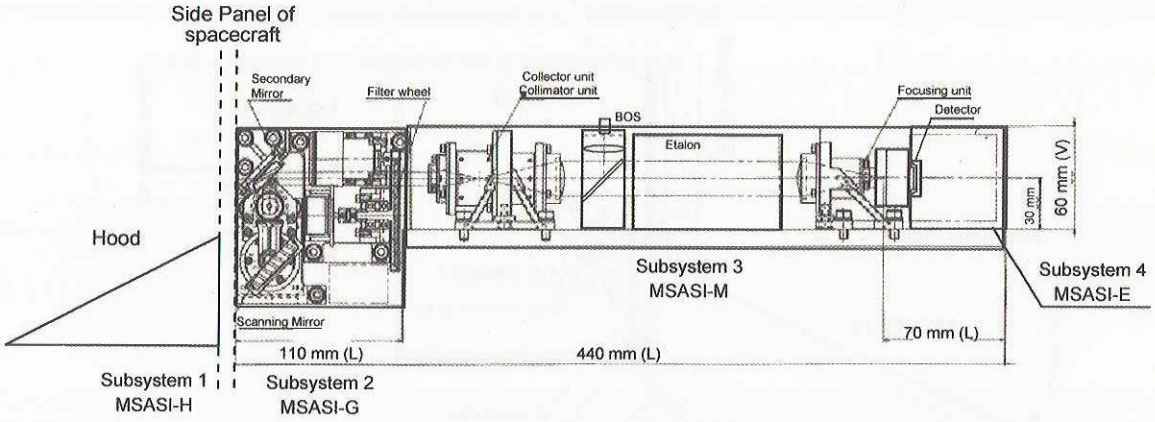

Figure 3.1: General layout of MSASI. MSASI consists of four subsystems (MSASI-H, -G, -M, and -E).

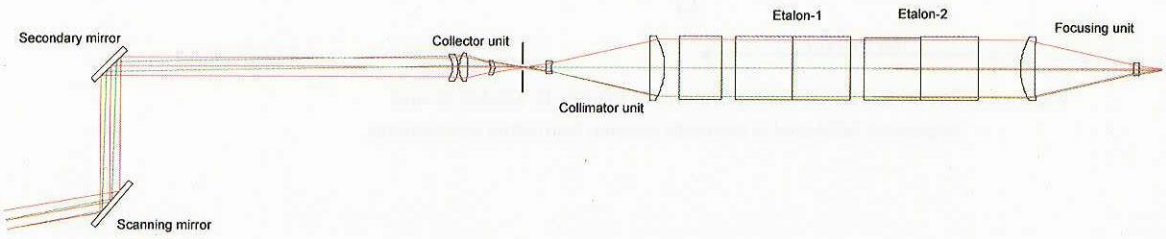

Figure 3.2: Optical layout of MSASI.

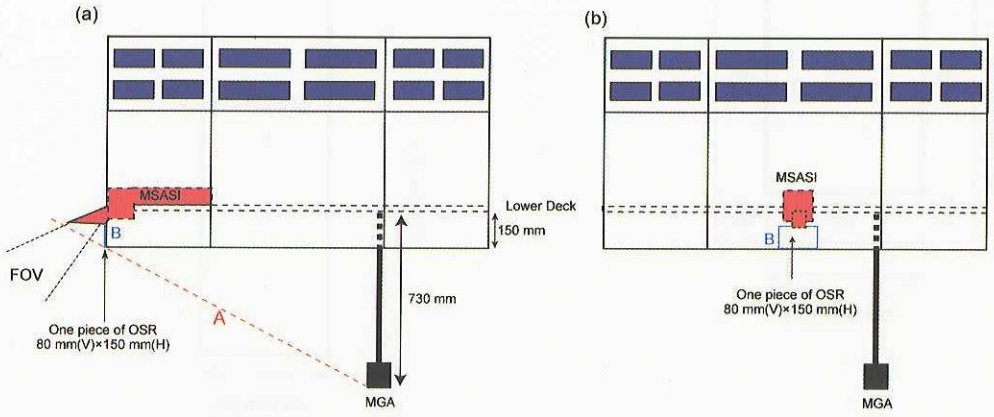

Figure 3.3: Installation of MSASI on MMO. It is required that any extensions and objects are behind the plane shown as a red-dashed line (Plane-A). To avoid random reflection on the side panel beneath the hood (Area B), it is necessary to place one piece of large OSR on this area.

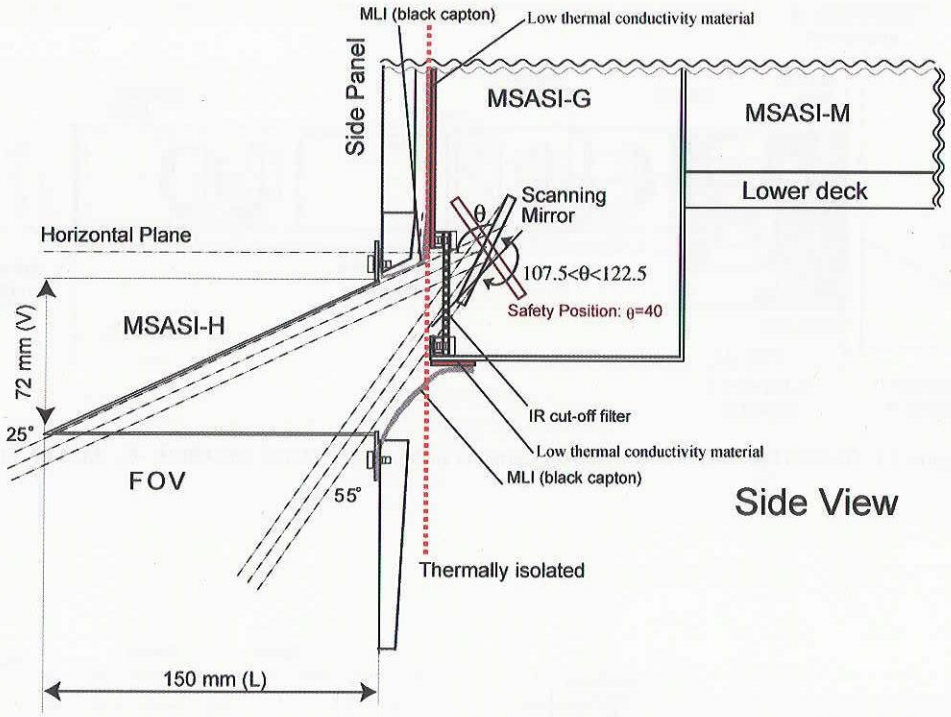

Figure 3.4: Cross-sectional configurations of MSASI-H, MSASI-G and MSASI-M. MSASI-H is thermally isolated from other subsystems.

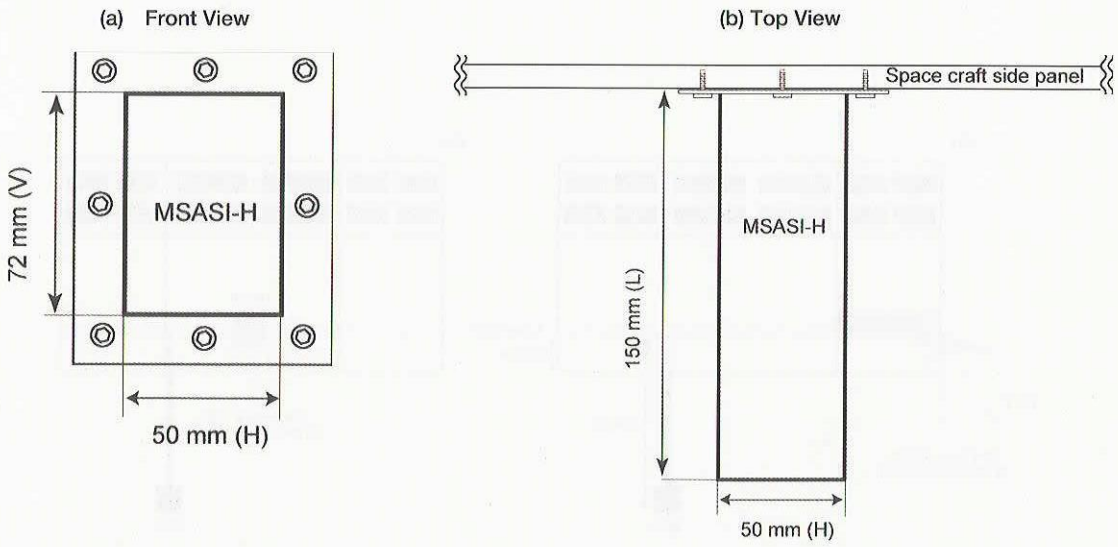

Figure 3.5: Length and shape of MSASI-H in current design. (a) Front view, (b) Top view.

3.2.3. Subsystem 2 : MSASI-G (Gearing system and front-optics)

Lead institution: IKI

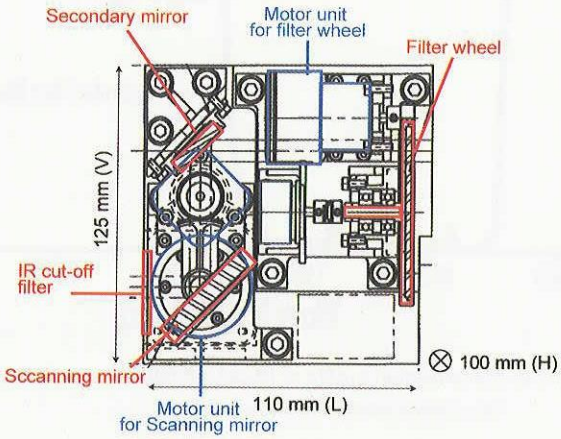

Figure 3.6: Cross-sectional diagram. The subsystem consists of IR cut-off filter, scanning mirror, secondary mirror, filter wheel, and motor drive units.

3.2.3.1 Subsystem 2-1: Scanning mechanism

The entrance scanning mirror rotates a field-of-view (FOV) of MSASI below the horizontal line from 25° to 55° [TBC] every 1° (15 steps), and has pointing accuracy and stability better than 0.1°. The mirror also works as an emergency cover of the instrument. When unexpected strong signals are detected by the bright object sensor (BOS) in MSASI-M, the mirror rotates to the safety position. In this position, no photon is introduced to the inside (see Figure 3.6).

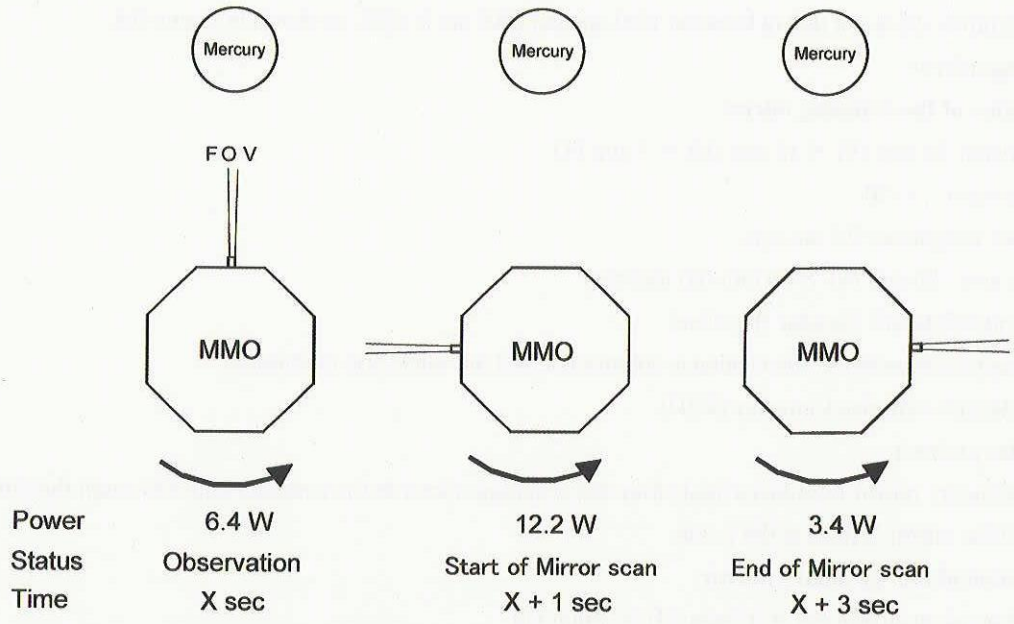

Figure 3.7: Schematic description of the timing of mirror scanning (top view). One sequence takes 2 seconds.

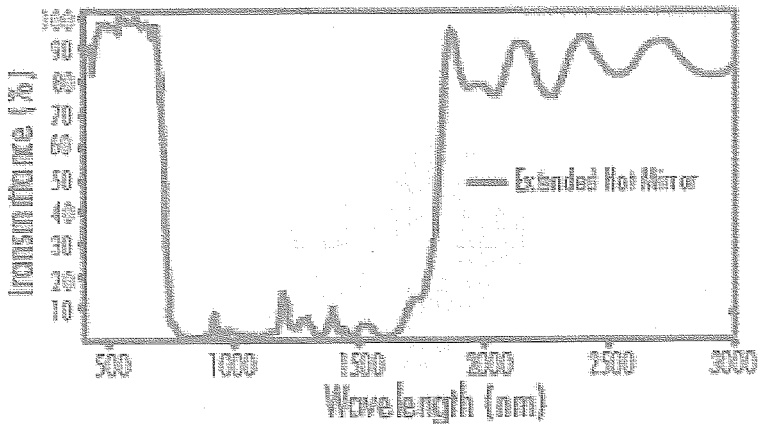

Figure 3.8: Transmission profile of IR cut-off filters (reflective type, http://www.edmundoptics.com).

● **Motor unit for scanning mirror**

A stepping motor with a harmonic gear achieves a stepping accuracy of 0.01°. Potentiometer and micro-switches measure the rotating position of the motor. They have good heritages in the past spacecraft missions (SELENE and Mars Express). One sequence (see Figure 3.7) takes 2 seconds. The sequence is completed, while Mercury is out of sight. The start timing (phase angle) is registered on MSASI-E before the observation. When the mirror scans 15 steps, the mirror moves to the initial position within 2 seconds.

● **IR cut-off filter**

A reflective type of infrared (IR) cut-off filter is installed at the entrance of this subsystem. Thermal inputs from the surface of Mercury (5.7 - 13.8 kW/m^2) longer than 750 nm are greatly reduced. Average reflection between 750 nm and 1150 nm is >95 % and that of between 1200 nm and 1600 nm is >85%, as shown in Figure 3.8.

● **Scanning mirror**

Specification of the scanning mirror

- Dimension: 35 mm (V) × 15 mm (H) × 7 mm (T)
- Shape error : λ /20
- Surface roughness: 0.5 nm rms.
- Active area : 30 mm (V) × 10 mm (H) aperture
- Substrate Material : Zerodur (baseline)
- Coating Characteristics: The coating is optimized at 589 nm (dielectric multilayer).
- Manufacture : Russian Company [TBD]

● **Secondary mirror**

The secondary mirror introduces lights from the scanning mirror to the common optics through the filter wheel. The angle of the mirror is fixed at the frame.

Specification of the secondary mirror

- Dimension: 20 mm (V) × 15 mm (H) × 5 mm (T)
- Shape error : λ /20
- Surface roughness: 0.5 nm rms.
- Substrate Material : Zerodur (baseline)

- Coating Characteristics: The coating is optimized at 589 nm (dielectric multilayer)
- Manufacture : Russian Company [TBD]

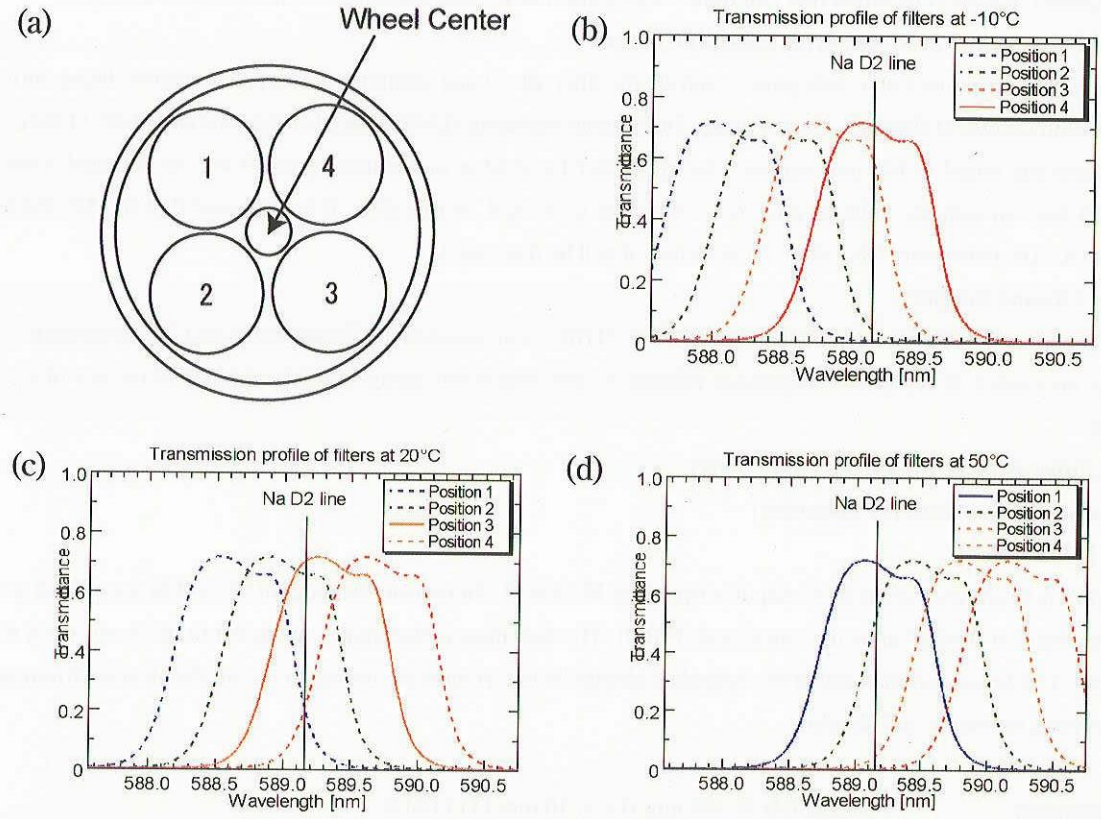

Figure 3.9: (a) Schematic description of the filter wheel. Each diameter of is 25 mm. The transmission of filter drifts at the rate of 0.018 nm/K around 589 nm. Transmission profiles at each temperature (b)-10, (c) 20° C, and (d) 50° C are shown. FWHM is 0.92 nm.

3.2.3.2. Subsystem 2-2: Filter wheel

The wheel compensates the filter for transmittance drift in wavelength due to temperature variation with selecting a corresponding filter.

- **Filter Wheel and Interference Filters**

As shown in Figure 3.9 (a), four interference filters are installed on the filter wheel. These filters prevent the unwanted orders of light from entering to MSASI-M. All filters have the same diameter of 25 mm, the same full width at half maximum (FWHM) of 0.92 nm, and different center wavelengths every 0.36 nm (588.70, 589.06, 589.42 and 589.78 nm at 20° C in vacuum). The FWHM of the filters are determined from the free spectral range (FSR) of the etalon-1 (Sub system 3-1) see section 3.2.4.2.

The operating temperature of MSASI ranges from -10° C to 50° C (see Section 5.3). The transmittance curve of an interference filter has dependency of temperature. The drift slope is 0.018 nm/K around 589 nm. By selecting an appropriate filter at corresponding temperature, MSASI can have wide operating temperature range from -10° C to 50° C. Figure 3.9 (b), (c), and (d) show example of wavelength shifts. For this purpose, house-keepnig (HK) data of the wheel temperature should be sent to MSASI-E in every minute.

● **Motor unit for filter wheel**

Good heritage motor, gear, potentiometer and micro-switches are used for driving the filter wheel (SELENE and Mars Express). It should be noted that two motor works alternative, that is, both never moves simultaneously.

3.2.3.3 Subsystem 2-3: Motor drive electronic board

The Motor drive electronic subsystem controls the filter wheel and scanning mirror, and ensures dialog with the MSASI-E (Subsystem-4) through a Low-Voltage Differential Signaling (LVDS) based serial interface (I/F) [TBD]. Size of the electronic board is 100 mm square. Electric power for driving motor units (+24 V) will be supplied from the spacecraft bus. To regulate voltage, a DC/DC converter is needed. In this state, it is supposed that the MSASI team provides DC/DC converter. After the A/O selection, it will be discussed.

3.2.3.4 Ground Support

A PC with serial interface (LVDS-based serial I/F [TBD]) and associated software to control the subsystem.

It is necessary to verify the alignment relative to the spacecraft using optical cube. An accuracy of 0.05° is required.

3.2.4. Subsystem 3: MSASI-M (Main body)

Lead institution: ISAS [PI institution]

3.2.4.1. Main Body

Figure 3.10 shows a cross-sectional description of MSASI-M. All optical elements of MSASI-M are placed on the baseplate made of A5052P alloy or honeycomb [TBD]. The baseplate is thermally connected to the lower deck of the spacecraft. Thickness and material of the baseplate should be determined according to the mechanical environment of the spacecraft (vibration and shock).

Dimension	: 60 mm (H) × 330 mm (L) × 10 mm (T) [TBD]
Substrate material	: Aluminium A5052P alloy or honeycomb [TBD]

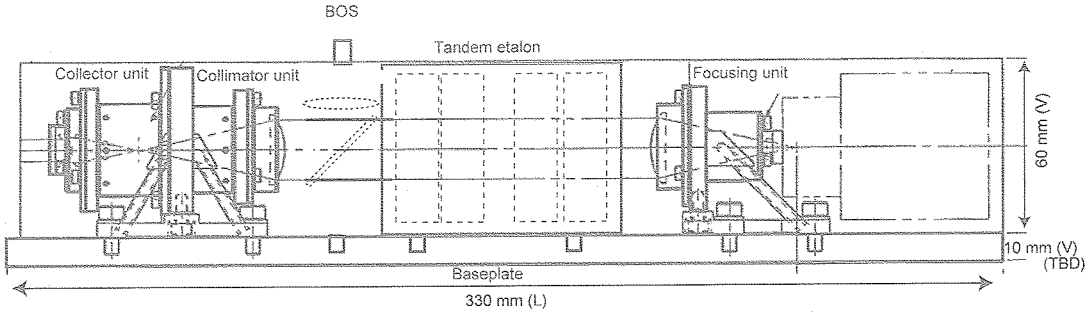

Figure 3.10: Cross-sectional diagram of MSASI-M. This subsystem consists of Fabry-Perot etalons, bright object sensor (BOS), common optics (collector, collimator and focusing units), beam splitter, and baseplate.

3.2.4.2. Subsystem 3-1: Fabry-Perot Etalons

Specifications of the etalon-1 and etalon-2 are summarized in Table 3.1. Substrates of etalons are made of fused silica, which is radiation-hardened optical glass. The surface flatness is better than $\lambda/200$. Dielectric multilayer, which is optimized for 589 nm reflection, is deposited on the surfaces of the substrates. The reflectivity of the multilayer is 94 %. In order to keep the constant spacing against the temperature variation (±30K), low expansion glass, Zerodur (thermal expansion coefficient: $\sim 0.5 \times 10^{-7}$/K), is used as a spacer material. The spacers and substrates are united with optical contacting technique (by inter molecular force).

Table 3.1: Specifications of the etalon-1 and etalon-2.

	Etalon1	Etalon2
Substrate	Fused Silica Diameter : 50 mm, Thickness : 15 mm	
Surface Flatness	Better than λ /200	
Effective Aperture	> 20 mm	
Mirror coating	Dielectric multilayer	
Reflectivity @ 589 nm	94 %	
Spacing	0.138 mm	0.868 mm
Spacer material	Zerodur	
FSR	1.255 nm	0.200 nm
FWHM	0.031 nm	0.005 nm
Finesse (FSR/FWHM)	~40	

The etalon-1 is characterized as smaller gap-spacing and wider free spectral range (FSR). This etalon determines a large envelope of the transmission wavelength of the subsystem. On the other hand, the etalon-2 has a larger gap-spacing and narrower FSR. This etalon determines the spectral bandpass (FWHM) of the subsystem (0.005 nm). The total transmission of the tandem etalon is shown in Figure 3.11. The etalon holder aligns two etalons in satisfactory way (0.01° accuracy) as shown a cross-sectional diagram of Figure 3.12(a). A photograph of each etalon, which was fabricated as a Bread-Board Model (BBM) in 2003 is shown in Figure 3.12(b). Performances of these etalons are shown in Figure 3.13.

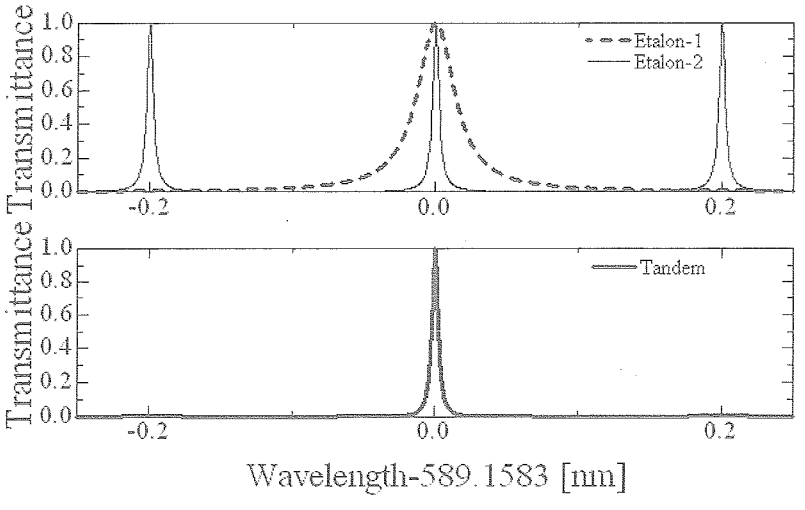

Figure 3.11: Upper panel: Transmission profiles of the etalon-1 (dashed line) and etalon-2 (solid line). Lower panel: Transimission profile of the tandem etalon (thick-solid line).

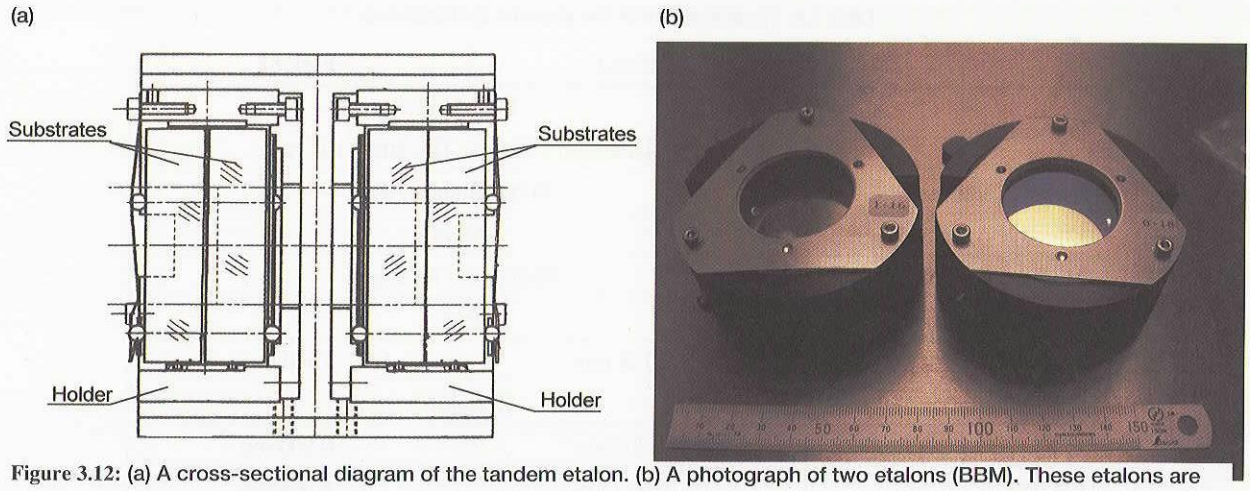

Figure 3.12: (a) A cross-sectional diagram of the tandem etalon. (b) A photograph of two etalons (BBM). These etalons are optimized for 632.8 nm (wavelength of He-Ne Laser).

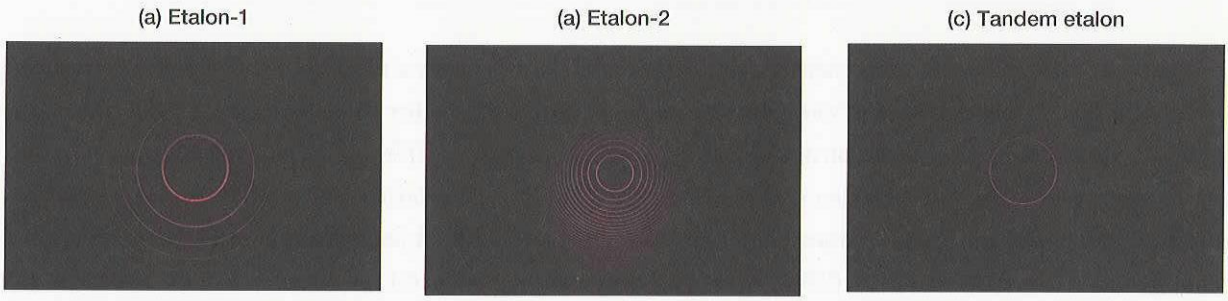

Figure 3.13: Alignment of the interference fringe. (a) Fringe image of the etalon-1. (b) Fringe image of the etalon-2. (c) Fringe image of the tandem etalon. This is a product of the innermost fringe of the etalon-1 in (a) and third fringe of the etalon-2 in (b).

3.2.4.3. Subsystem 3-2: Common Optics

The common optics consists of collector, collimator and focusing units. Table 3.2 shows parameters of the three units. The total length of the optics is 245 mm. As shown in Figure 3.14, the tandem etalon (subsystem-3-1) are installed between collimator and focusing units. A field of view (FOV) of the MSASI-M is 1° (half angle). Calculated spot diagram is shown in Figure 3.15. Each spot is small enough, at the most 10 μm that corresponds to a pixel size of detector. Also, the defocusing, which is arisen from the mechanical misalignment, is allowed by $\pm$ 10 μm.

The focal length in vacuum is estimated to be shorter than that in the atmosphere by 137 μm. To compensate this difference, two sims are used alternatively depending on the test purposes.

In order to avoid the transmittance degradation of glass due to the solar radiation, the optics employs Fused silica and non-browning glass (small amount of CeO_2 is contained). A result of irradiation test (9.1 MeV proton; 230 krad) for non-browning BK7 (contains 1.2% CeO_2) is shown in Figure 3.16 (Misawa *et al.*, 2002b). A total dose of 230 krad is a factor of 3 larger than estimated total dose of MMO during the mission. It is clear that transmittance shows little change (600 nm : from 91.9% to 90.9%; 750 nm : from 90.1% to 90.1%).

A bright object sensor (BOS) is located (Figure 3.14) between collimator unit and tandem etalon. A beam splitter reflects a small part of incident light (~3%) toward the BOS. MSASI-E digitizes the signal from BOS by 10-bit. When unexpected brightness above the registered threshold level is detected by BOS, MSASI-E shuts down the High

Voltage (HV) units for the image intensifier. Just after the shut down of the HV unit, scanning mirror is changed to the safety position.

Table 3.2: Parameters of each part of the common optics.

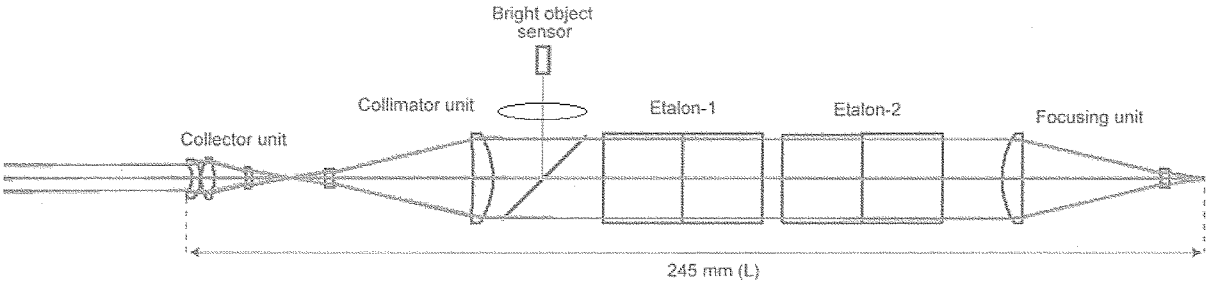

Figure 3.14: Cross-sectional image of MSASI-M.

	Aperture	Focal Length
Collector Unit	6.6 mm	20 mm
Collimator unit	20 mm	60 mm
Focusing unit	20 mm	60 mm

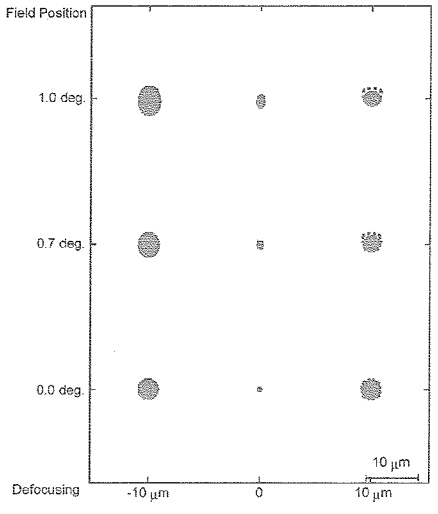

Figure 3.15 Spot diagram of the optics in MSASI-M with respect to the field and defocusing positions. Spots are smaller than pixel size of CMOS sensor.

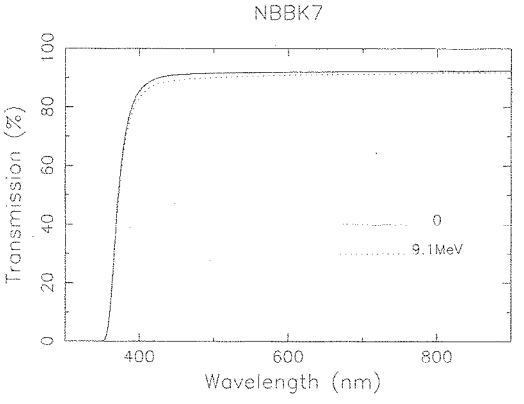

Figure 3.16: Transmittance of non-browning BK7. Solid and dotted lines show the transmission before and after 9.1 MeV proton irradiation (230 krad), respectively. Little degradation is seen in longer than 550 nm (600 nm : 91.9%→90.9%; 750 nm : 90.1% → 90.1%, Misawa *et al.*, 2002b).

3.2.5. Subsystem 4: MSASI-E (Electronics and Detector)

Lead institution: ISAS [PI institution]

MSASI-E is placed on the baseplate of MSASI-M by sims to adjust the focal position of the detector.

MSASI-E is manufactured by Meisei Co.

3.2.5.1. Sub system 4-1: Electronics Boards

The electronics boards consist of 5 pieces of 60 mm square boards, 1) High voltage units, 2) Field Programmable Gate Array (FPGA) and memory, 3) driver for a CMOS/Active Pixel Sensor (APS), 4) external Analog-Digital convertor (ADC) unit for CMOS/APS, and 5) LVDS I/F.

3.2.5.1.1. S/C Interface handling

- The subsystem-4 performs processing image data, spacecraft interface, telecommand and stamping, telemetry, sending signals to MSASI-G, controlling the HV unit, receiving signals from MSASI-M (BOS) and collecting house keeping data. Figure 3.17 shows detailed diagram of MSASI-E and its electrical connection between other subsystems.

It is the single interface to the spacecraft (LVDS-based serial I/F [TBD]). Figure 3.18 shows block diagram of MSASI. All electrical parts are Class-B. We require phase clock (11-bit required) for start timing of read-out.

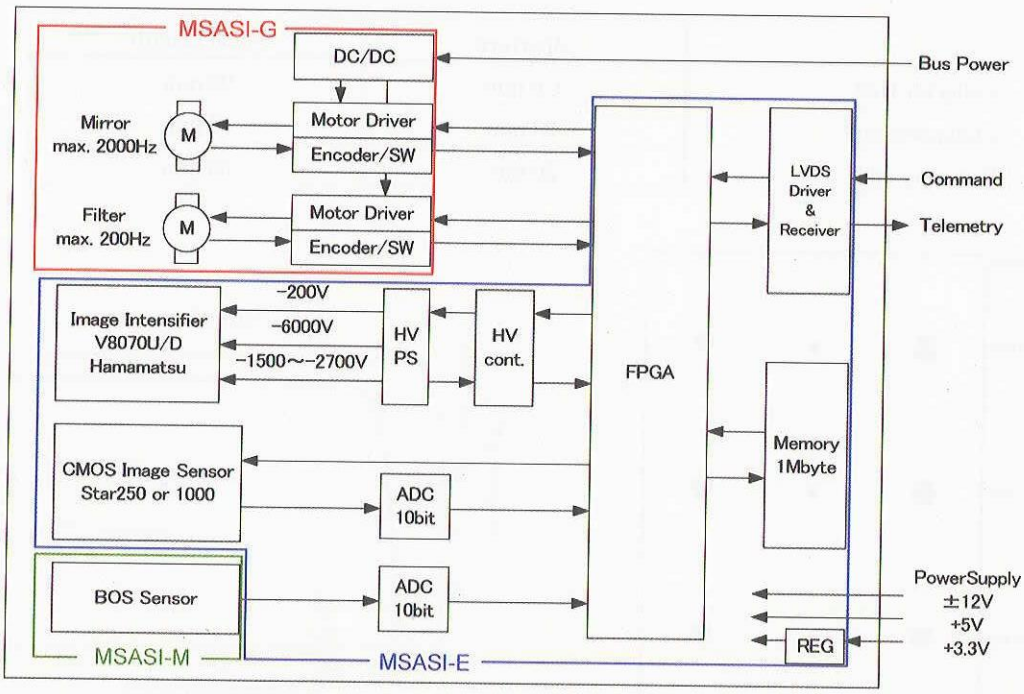

Figure 3.17: Detailed diagram of MSASI-E, MSASI-M and MSASI-G.

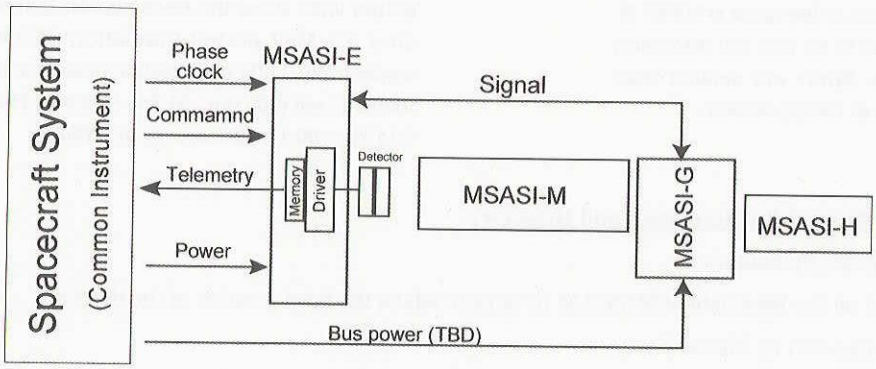

Figure 3.18: Block diagram of MSASI.

3.2.5.2. Subsystem 4-2: Detector unit

The detector unit consists of an image intensifier and CMOS/APS. They are coupled with a fiber optic plate (FOP). Intensified signals are detected by the CMOS/APS by way of FOP.

3.2.5.2.1. CMOS/APS (Active Pixel Sensor)

The radiation hardened CMOS/APS, STAR-1000 (Fillfactory), is used as a detector. Specification of STAR-1000 is shown in Table 3.3. We select the region of interest (ROI) of 10 × 10 pixels among 1024 × 1024 pixel array with a pixel size of 15 μm square.

For ROI mode, readout-time increases according to the number of readout columns and lows. In the case of 10 × 10 pixels readout, every 20 μs (50,000 frames-per-sec) read-out is possible. This fast readout method is used for photon-counting mode (see section 9.3.1).

The external A/D circuit (10-bit) with the correlated double sampling (CDS) logic is used to minimize a readout-noise.

Table 3.3: Specification of STAR-1000.

Pixel array (pixel size)	1024 × 1024 (15 μm)
Readout noise	35 electrons
Quantum efficiency × fill factor	~25% @ 530 nm
Readout frequency (Full frame)	14 frames-per-second
Total doze Radiation tolerance	> 230 krad (Si)

3.2.5.2.2. Image Intensifier

The image intensifier (I.I.), V8070U/D, which has two-stage micro channel plate (MCP), is provided by Hamamatsu Photonics co. ltd. We operate it at the gain of 10^4. A GaAsP photocathode realizes the quantum efficiency up to 50% at 589 nm. A phospor, Hamamatsu P46, has a short light duration time (1 μs). The phospor can convert an electron to 20 photons around 530 nm in wavelength. That is, one incident photon is amplified to $2x10^5$ photons at 530 nm. These photons are transferred through the fiber optic plate (FOP) to CMOS/APS.

3.2.5.2.3. High voltage (HV) Unit

High voltage units for control of the I.I., EMCO Q02 -5 (-200 V; for MCP-in), Q40N-5 (-4000 V; MCP gain control: variable) and Q60N-5 (-6000 V; for MCP-out) are used. Applied voltage on MCP is controlled by 256 steps (8-bit) between -1500 and -2700 V.

As soon as BOS releases the emergency signal, the HV units are shut down.

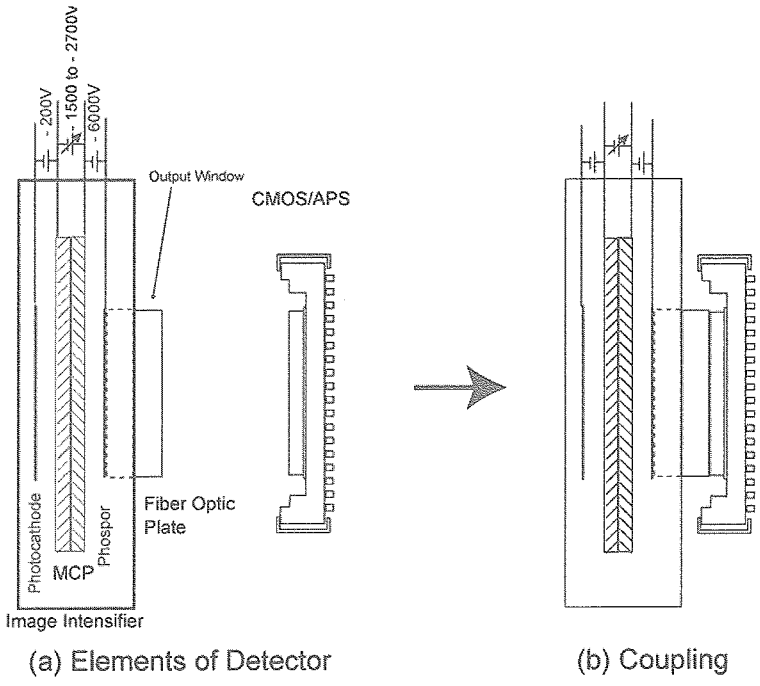

Figure 3.19: (a) Detector components. Image intensifier (I.I.), fiber optic plate (FOP) and CMOS/APS. (b) The output window of the I.I. and the CMOS sensor are directly coupled with a FOP.

3.2.5.2.4. FOP Coupling

CMOS/APS and I.I. are connected via a fiber optic plate (FOP) coupling method. A diameter of each fiber is 6 μm. Figure 3.19 shows schematic images of the FOP coupling. The coupling process is done by ISAS with the support of Fillfactory Co. To avoid reflections at the boundary between FOP and surface of the CMOS/APS, the epoxy bond with relatively close refractive index to FOP is used. The radiation tolerance of the epoxy bond will be tested.

3.2.5.3. Subsystem Ground Support Equipment

A PC with serial interface (LVDS-based serial I/F [TBD]) and associated software to control the subsystem.

3.3. Instrumental heritage and maturity

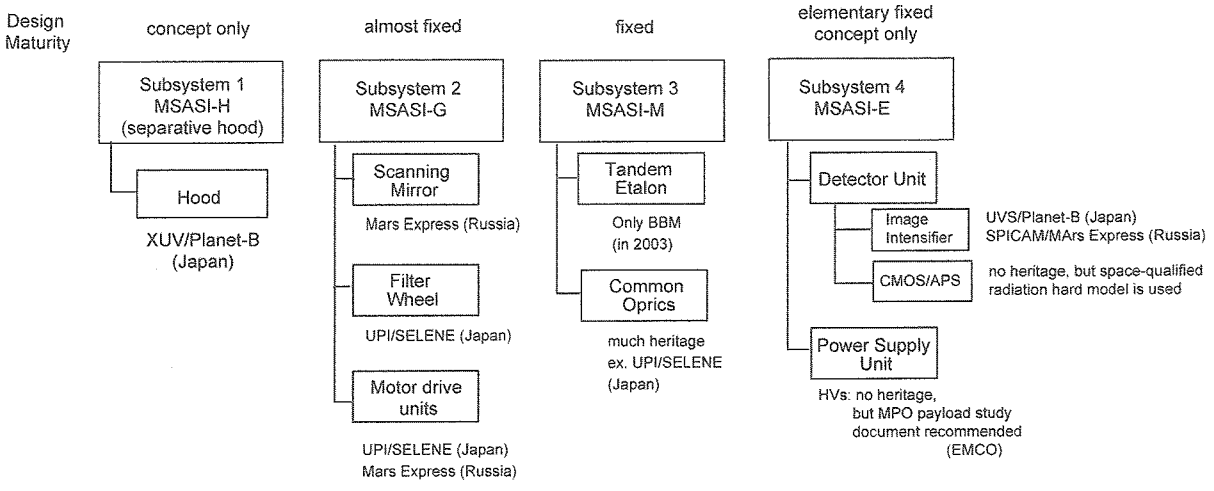

Figure 3.20: Heritage and Maturity of each subsystem.

4. Resource Budgets

Power consumption (in Watts):

The two motor works alternatively.

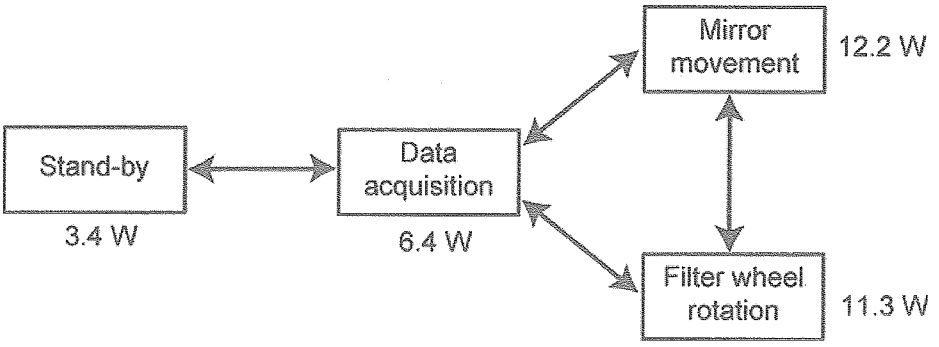

Figure 4.1: Block diagram of power consumption.

Table 4.1: Power consumption of each part (unit: W)

	+12 V	-12 V	+5 V	+3.3 V	Bus	Total [W]
Common			1.00	0.30		1.30
BOS	0.01	0.06	0.03			0.10
CMOS	1.00	0.60	0.40			2.00
HV		0.08	2.92			3.00
motor driver			0.20			0.20
motor1 (Mirror)					5.60	5.60
motor2 (Filter)					4.70	4.70

Table 4.2: Power consumption of each state (unit: W)

	Common	BOS	CMOS	HV	motor driver	motor1 (Mirror)	motor2 (Filter)	Total [W]
Standby	1.3	0.1	2	0	0	0	0	3.4
Data acquisition	1.3	0.1	2	3	0	0	0	6.4
Mirror movement	1.3	0.1	2	3	0.2	5.6	0	12.2
Filter rotation	1.3	0.1	2	3	0.2	0	4.7	11.3

Mass (in grams):

Table 4.3: Estimation of mass of each subsystem.

MSASI-H		MSASI-G		MSASI-M		MSASI-E		Total
Hood	80	Flat mirrors	20	Slit assembly	100	Image Intensifier	110	
OSR	20	Mirror Holders	161	Lenses	15	CMOS/APS	100	
		Scanning mechanism	191	Lens Holders	371	HV units	35	
		Filter wheel mechanism	251	Etalons	280	Electric board	250	
		IR cut-off filter	20	Etalon holders	280			
		Electronics board	250	BOS	10			
		(including DC/DC conv.)		Baseplate	650			
		Baseplate	200	Cover	90			
		Cover	70					
	100		1163		1796		495	3,554

(Including DC/DC converter)

5. Summary of Experiment Interfaces

5.1. Mechanical interfaces

Volume : 60 (H) × 70 (V) × 330 (L) mm (MSASI-M, including MSASI-E)
100 (H) × 125 (V) × 110 (L) mm (MSASI-G)
50 (H) × 72 (V) × 150 (L) mm (MSASI-H; TBR)

5.2. Optical interface

5.2.1. Pointing

Pointing accuracy of MSASI with respect to the reference frame of the spacecraft should be verified using alignment cubes (0.05° accuracy).

5.2.2. Field of View

MSASI-M has its own field-of-view (FOV) of 2° (latitudinal, perpendicular to the spin axis) × 2° (longitudinal, parallel to the spin axis). The scanning range of the mirror is 15° that corresponds to total FOV of 30° along the vertical direction.

5.3. Thermal interfaces

The temperature ranges of MSASI are as follows:

- Operating temperature: -10° C to +50° C
- Standby temperature: -20° C to +75° C.
- No cooling required for the detector.

Figure 5.1 shows model calculation of the temperature variations of the baseplate and lens in MSASI-M and the lower deck of MMO. MSASI is always within the operating temperature (between -10° C and +50° C). Figure 5.2 shows the case at perihelion. Although it is the worst case study for MSASI, MSASI-M keeps the operating temperature during most part of the orbit. Therefore, MSASI can carry out the observation during all orbital phase after the insertion except for very short interval at perihelion.

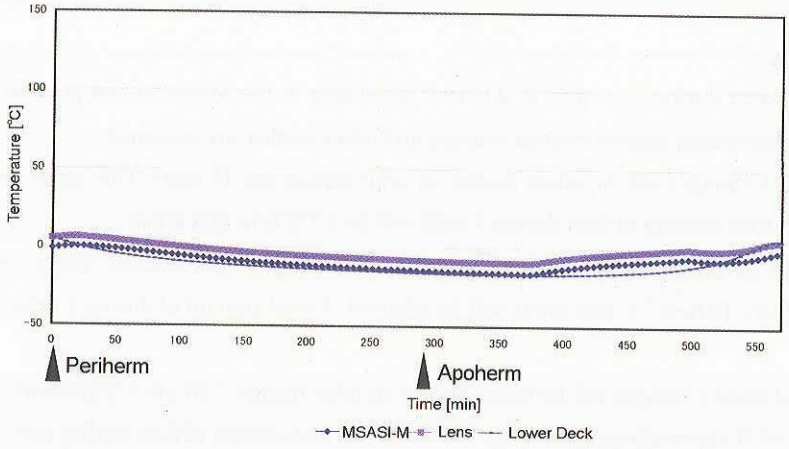

Figure 5.1: Temperature variation of MSASI-M, lens and the lower deck of MMO during one orbit. Temperatures range from -10° C and 0° C.

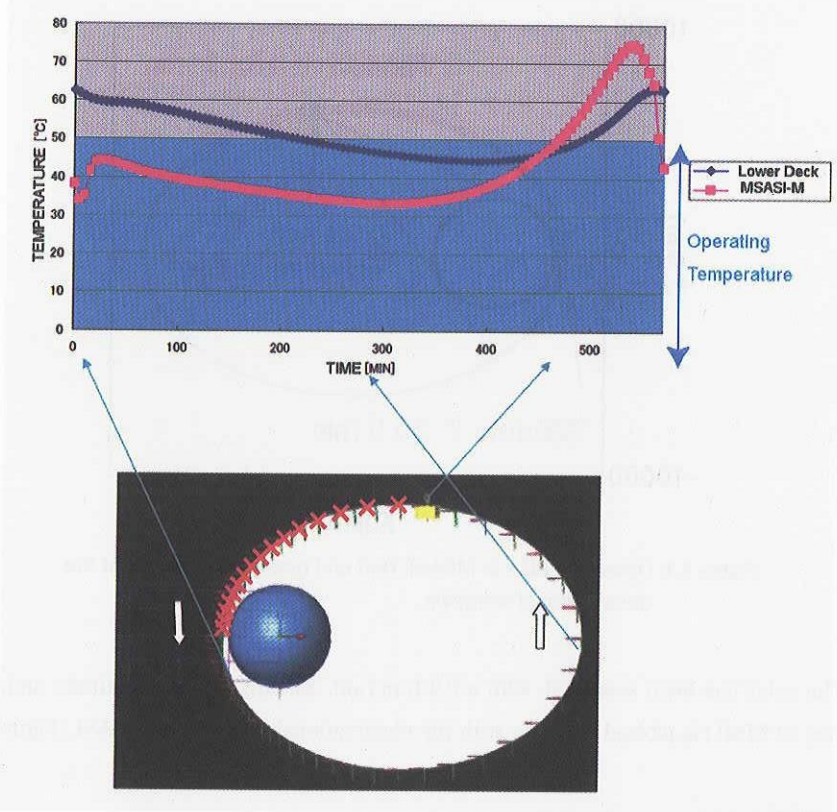

Figure 5.2: Thermal model calculation of MSASI-M in the case of perihelion of Mercury (worst case). (Top) Temperature variations of the lower deck of MMO and MSASI-M. MSASI keeps the operating temperature during most of orbit even for the worst case. (Bottom) An orbit of MMO at the time of calculation. Red crosses mean that MSASI is out of range of the operating temperature.

5.4. Data interfaces

5.4.1. Observations

Total amount of data during one orbit is different according to the observational priority relative to the other instruments. Three observation modes, normal, camera and other modes, are assumed.

In **normal mode,** 10 images will be taken during an orbit (image per 15 min). This mode will be usually adopted during the mission. A total amount of data during 1 orbit will be 3.2 Mbyte (0.8 kbps) .

In **camera mode,** 30 images will be taken during an orbit (image per 5 min). When priority of the MSASI observation is high (e.g., TAA=65°), this mode will be adopted. A total amount of during 1 orbit will be 9.6 Mbyte (2.4 kbps).

In **other mode,** at most 5 images will be taken during an orbit (image / 30 min). This mode will be adopted when the priority of the MSASI observation is low. (e.g., TAA=180°) Total amount of data during one orbit will be 1.6 Mbyte (0.4 kbps).

5.4.2. Operations

5.4.2.1. Data Rate without Compression

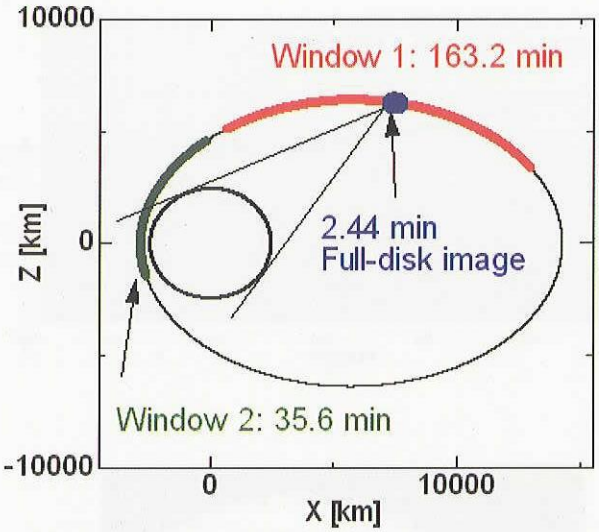

Figure 5.3: Operation plan of MSASI: Red and green lines represent the observational windows.

Data rate : The orbit has been assumed, with a 9.3 h period, 400 km periherm altitude and 12,000 km apoherm altitude. A trajectory of MMO is plotted together with the observational window for MSASI (Figure 5.3).

・Mercury is in FOV

(red and green lines in Figure 5.3): 3.31 h/orbit

Window-1: Exosphere observation

163.2 min/orbit = 2.72 h/orbit

163 exosphere images/orbit (max; 1 image/min)

Full-disk of Mercury is in FOV

(blue line in Figure 5.3) 2.44 min/orbit

2 full-disk images/orbit

Window-2: Limb or topographic (optional) observation

35.6 min/orbit = 0.59 h/orbit

35 limb images/orbit (max)

Science:

	Normal mode	Camera	Other	HK
Data acquisition per spin	10*10*178*10			every 4 sec ・Rotary encoder ・High voltage every 60 sec Temperature (filter wheel, etalon, CMOS and electric board) **34 [byte/min]**
Mirror scan	15 [steps]			
Images [/ orbit]	10 [images]	30 [images]	5 [images]	
Total Data [/orbit]	10*10*178*10*15*10 **=26,700,000 [bit]** **= 3,260 [Kbyte]**	10*10*178*10*15*30 **=80,100,000 [bit]** **= 10,013 [Kbyte]**	10*10*178*10*15*5 **=13,350,000 [bit]** **=1,669 [Kbyte]**	
Data rate (average)	0.8 kbps	2.4 kbps	0.4 kbps	4.5 bps

House keeping (HK):

If possible, regulated voltages and currents of +12 V, -12 V, +5 V, and +3.3 V are necessary.

Yearly Science Data volume:

Observation:

Normal mode	Camera mode	Other mode
3,260 Kbyte * 24/9.29 * 365 =	10,013 Kbyte * 24/9.29*365=	1669 Kbyte * 24/9.29 * 365 =
3,099 Mbyte/ year	9,221 Mbyte/year	1537 Mbyte/year
+ 20% margin	+ 20% margin	+ 20% margin
3,719 Mbyte/ year	**10.8 Gbyte/year**	**1,844 Mbyte/year**

HK : 34*24*60*365 = **17 [Mbyte/year]**

5.4.2.2. Data Compression Logics

- As a baseline, lossless data compression technique based on entropy coder is used. Expected data compression ratio is not so high, 30-50% in general.
- Basically Lossy data compression technique is not used. Instead, binning of 2 or 3 pixels in spatial direction and/or a long integration will be used to reduce the number of images.

6. Requirement for MMO system

1. Requirement of MSASI-H location; it causes stray lights problem.
2. Phase clock pulse is necessary.
   11-bit (=every 2msec) is required.
3. Contamination control during Assembly Integration and Verification (AIV)
4. Pointing accuracy keeps better than 0.01° . It should be checked after the installation.

7. Test and Calibration Plan

7.1. On-Ground test and Calibration plan

We will conduct on-grounding test in following categories:

A. Sub-system level test

This test is performed at each lead institute, as a bench test, supported by the sub-system E-GSE.
EM of PCS/DPU is necessary.

B. Overall instrument (MSASI) level test

This test is performed on the integrated MSASI, supported by all E-GSEs.
A DPU emulator (EM of PCS/DPU) is necessary.

C. System level test

With the instrument installed on the spacecraft, the E-GSE will support for analysis of test date, received from the Central Checkout System.

Major tests specified for MSASI are as follows:

A. Sub-system level test

[Optical test]

A sufficiently large vacuum chamber will be used for testing each optical component. Hollow cathode sodium lamp is used as a light source. Spectral and special resolutions, detector sensitivity, and defocusing length are calibrated.

Table 7.1: Test schedule plan of MSASI.

Content				Test Schedule					
			EM						
			FM				2006/9	2006/9	2006/
			Test level	Initial Performance Test	Thermal Cycle Test @TBD	After Thermal Cycle Test @Nikon	Vibration Test @ ISAS	After Vibration Test @Nikon	Thermal Vacuum Test @ ISAS
Optical performance	1	Focal length	A	○					
	2	Effective Aperture	A	○					
	3	Field of View	A, B	○					
	4	Total transmission rate	A	○					
	5	Spot diameter	A, B	○		○			○
	6	Focal position	A	○					○
Mechanical Performance	7	Function	A, B	○		○	○	○	○
	8	Strength	A		○		○		
	9	Characteristic	B				○		
Physical performance	10	Over view	A,B	○		○	○		○
	11	Size, weight and position of the center of gravity	A, B	○					
Electronics Test	12	Electrical Function, detector noise	A, B	○				○	○

[Electrical test]

The electrical test will be performed on MSASI-G and MSASI-E.

- **Function test:** The MSASI team checks the performance and function of the MSASI system. Interface with DPU (EM), data sorting and handling, detector drive, and emergency sequence (MSASI-E), and gearing movement and function (MSASI-G) are tested.
- **Calibration test:** The MSASI team collects calibration date for converting digital data to physical values. Dark noise and readout noise of the detector, and exposure time (MSASI-E) are calibrated. The data is used to calibrate measurements in space.

[Mechanical test]

MSASI-G will do the motor drive test under vacuum and atmosphere.

[EMC test]

MSASI-G and MSASI-E will participate in the EMC test as sub-system level test, if requested. In the case, the

MSASI team should make detailed negotiations with the other PIs and MMO system team for the resource and sequence for the testing.

B. Overall instrument (MSASI) level test

The integrated MSASI is tested in vacuum. ISAS is equipped with a vacuum chamber, volume 120 litters, which will be used for testing each optical and mechanical component. This facility also has 3-axis and 2-rotational stages and hollow cathode sodium lamp.

Checkpoints follow:

1. FOV
2. Spot diameter (spectral resolution)
3. Mechanical function
4. Electrical function
5. Overall sensitivity

C. System level test

-Alignment

During integration, the alignment of the optical axis of the instrument with the reference frame of the spacecraft will be measured with an accuracy of 0.05°, using alignment cubes. The alignment will be verified in flight, during cruise or in orbit, by the observation of a star; any offset which might have built up during vibrations at launch between the reference frames of the S/C (defined by its stellar sensor) will be measuredaccurately by analyzing instrument data, and taken into account for the scientific observations.

- Function test

Same as MSASI level test

- Calibration test

The MSASI team checks the dark and read-out noises, overall sensitivity, and spectral resolution, using the Hollow cathode sodium lamp.

7.1.1. Facilities

-EMC	ISAS/JAXA (Japan)
-Vacuum/Thermal Vacuum	ISAS/JAXA (Japan)
-Mechanical environment tests	ISAS/JAXA (Japan), IKI (Russia)
-Optical test	ISAS/JAXA, NIPR (Japan)

7.2. Cruise and In-Orbit calibration

- Spectral response (Moon Calibration Mode)

It will be necessary to regularly calibrate the spectral response of the MSASI detectors and optics during Moon flyby phase. Fraunhofer absorption line reflected from the surface of the Moon and sodium emission from lunar exosphere are used as calibration sources. When Moon is in FOV, Fraunhofer absorption line becomes a calibration source. On the other hand, when limb of the Moon is in FOV, sodium emission becomes a calibration source.

-Alignment

By the observation of a star; any offset which might have built up during vibrations at launch between the reference frames of the S/C (defined by its stellar sensor) will be measured accurately by analyzing instrument data, and taken into account for the scientific observations.

8. Requirement for AIV test

The instrument must be kept in clean conditions (cleanness less than 100,000; TBR) during all the AIV phases.

9. Flight Operations Concept

9.1. Initial Operation

The MSASI team expects following operations in Earth orbiting, Cruising, and Initial Mercury Orbiting phases.

1) Earth orbiting phase

- Initial Health Check

Overall health check of MSASI will be executed before the Cruising phase start.

[by MSASI team]

- Moon Observation [optional]

To calibrate wavelength and intensity response of the detector and also to obtain scientific return, observations of the Moon will be carried out.

[by MSASI team]

2) Cruising phase

- Short Health Check

Short health check of MSASI will be executed. Intervals will be negotiated with the MMO System Team and other PI teams. **But motor units should be check once a week at least.**

[by MSASI team]

3) Mercury Orbiting Phase

- Initial Health Check

Overall health check of MSASI will be executed just after the Mercury Orbit Insertion.

[by MSASI team]

- Initial Observation Check

Initial observation check of MSASI will be executed.

[by MSASI team]

- Alignment Check [optional]

Verification of optical alignment will be carried out using star observations.

9.2. Normal Operation

In normal operation in Mercury Orbiting phase, MSASI will work under the integrated control of DPU in cooperation with other in-situ plasma measurement (i.e. particles and magnetic field).

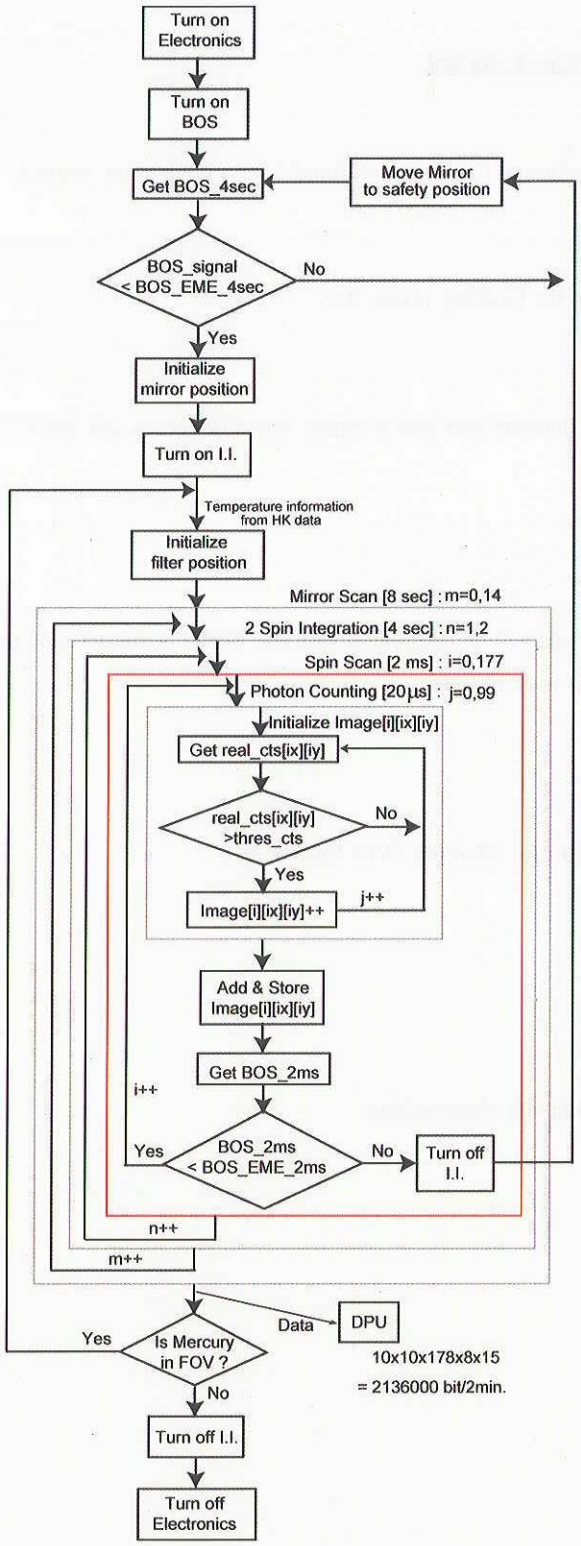

Figure 9.1: Sampling logic of MSASI in the case of the photon-counting mode.

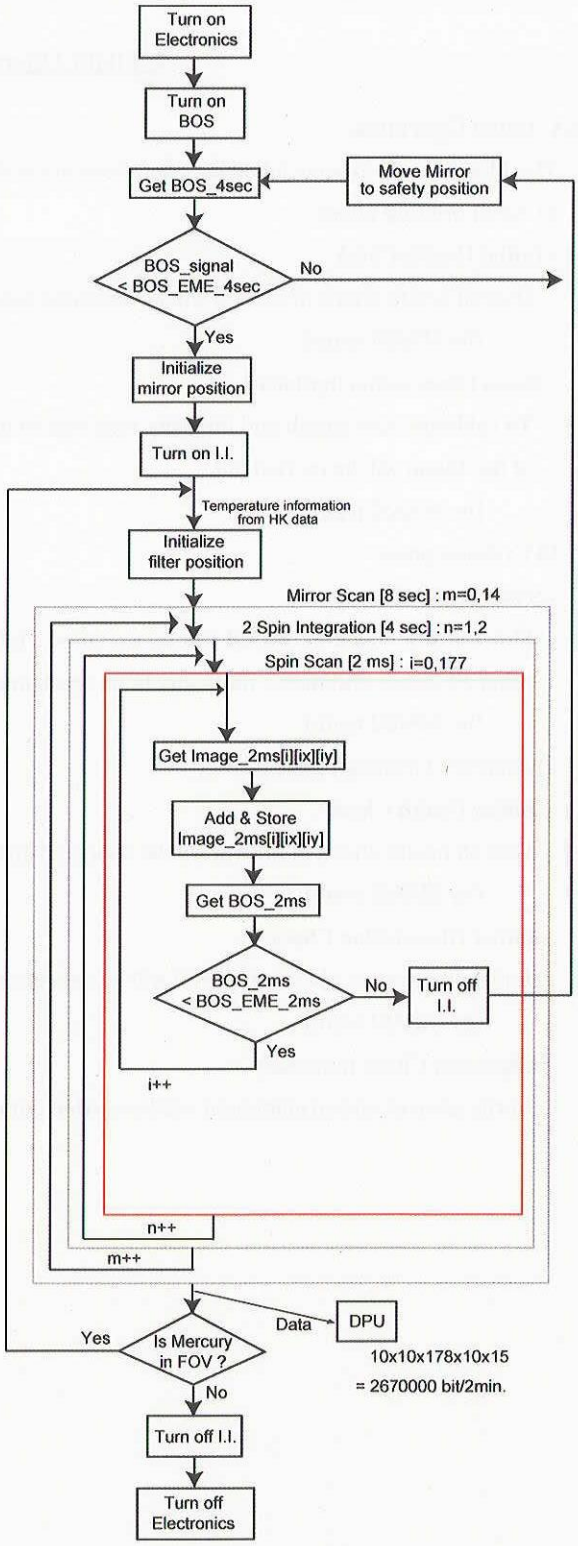

Figure 9.2: Sampling logic of MSASI in the case of the integration mode.

9.3. Observation Modes

Two modes of observation will be used. The photon-counting and integration modes are selectable. **It should be noted that no additional load and task are needed in S/C and DPU. Both modes require DPU** to pick up MSASI scientific data every 1 or 2 minutes from the memory in MSASI-E (see Figure 9.1 or 9.2).

9.3.1. Photon-counting Mode [mapping of low intensity region]

A sampling logic of the photon-counting mode is shown in Figure 9.1.

- **Function of BOS**

Before the observation, BOS verifies no unexpected bright object within FOV of MSASI.

During the observation, if unexpected bright object appears in FOV, BOS sends emergency signal to MSASI-E directly, then HV units are immediately shut down and the scanning mirror rotates to the safety position.

- **Initialize mirror position**

The scanning mirror rotates to the initial position, if it was held at the other position.

- **Turn on I.I.**

MSASI-G turns on HV units applied to I.I.

- **Initialize filter position**

The filter wheel sets the appropriate filter.

- **Photon-Counting**

Selecting area (10 × 10 pixels) (**real_cts[ix][iy]**) are read out every 20 μsec. Only if a signal from each pixel exceeds a certain threshold level (**thres_cts**), event number of 1 is added to **image[i][ix][iy]** (ix, iy are coordinates (1-10), i is labelled every 2 msec). This procedure will be carried out 100 times during 2 msec. This event data will be generally treated as 10 bit.

- **Spin Scan**

Spin Scan of 2 msec exposure, which consists of 100 times of photon-counting, is carried out 178 times during a spin. It corresponds to 30° covering the Mercury disk.

- **N Spin Integration**

(In this figure, n is assumed at 2.) After 2-spin scan is carried out, the scanning mirror rotates by one step. Event data is integrated every 2 spin.

- **Mirror Scan**

The scanning mirror rotates to the next position, and to up 15th position.

9.3.2. Integration Mode [mapping of high intensity region]

Figure 9.2 shows a sampling logic of the integration mode. Most are the same as the photon counting mode. Signal is accumulated during 2 msec and read out every 2 msec. Data is digitalized by 10-bit.

Figure 9.3 shows the SN ratio for observations.

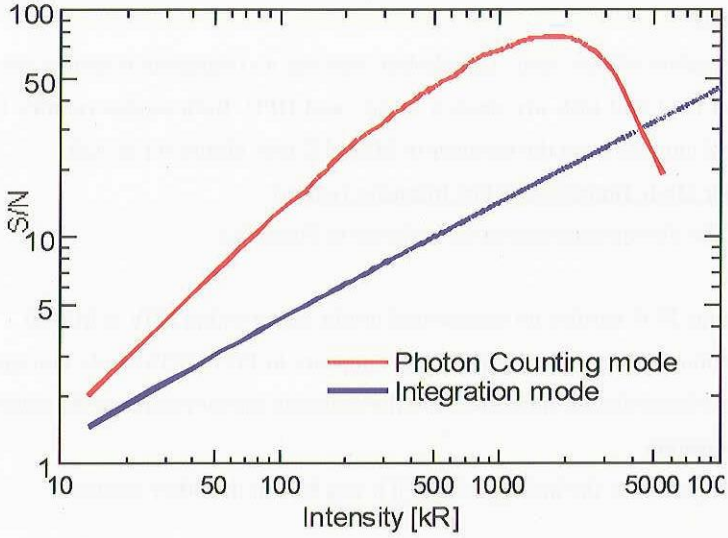

Figure 9.3: SN ratio for observations.

10. Scientific Data Reduction and Analysis Plans

10.1. Scientific and Auxiliary Data Products

During the mission, Level 1 data (including the original scientific and auxiliary orbit, attitude, and spacecraft status information) will be distributed from the JAXA/BepiColombo Project Office.

The MSASI team will perform the data reduction and calibration of the MSASI data. The product, Level 2/3 data sets, will be distributed to JAXA and the MSASI team members.

JAXA will distribute the level 2/3 data to the BepiColombo Project Team.

10.1.1. Level 1: Raw telemetry data

Spectral imaging data

MSASI house keeping (HK) data

10.1.2. Level 2: Calibrated data

Spectral imaging data

MSASI HK data

10.1.3. Level 3: Summary Plots of Level 2 data

Spectral imaging data

MSASI HK data

10.2 Data Processing and Analysis Concept

Exclusive data rights reside with the MSASI team for a maximum of 6 month from receipt of the Level-1 data. After this time, Level-2/3 data will made available to the BepiColombo Science Working Team members at large through the ESA-JAXA science data archive.

Data processing and analysis will be mainly done by ISAS/JAXA , Tohoku University, and IKI.

Scientific results from MSASI will be published, in a timely manner, in appropriate scientific and technical journals. Proper acknowledgement of the services supplied by ESA and JAXA will be made.

The MSASI team will provide JAXA with processed and useable data for Science Communication purposes as soon as possible after their receipt.

10.3. Specific Requirement of Infrastructure and Hardware to ISAS/JAXA

For the compliance of Sec. 10.2 (especially for "6 month" exclusive data right), Japanese MSASI team request the provision of human resource, hardware, and software support for the data reduction to the JAXA/BepiColombo Project Office.

10.4. Compliance with Science Data Policy in the MMO Science Management Plan

The MSASI team, under responsibility of PI, will comply with the scientific data policy of ESA and JAXA as defined in the MMO Science Management Plan (MMO-SMP), including the data format definition.

Acknowledgements. The authors would like to thank all the members of the MSASI team and the members of the BepiColombo/MMO mission for a lot of suggestions and advices.

References

[1] Barbieri, C., C. R. Benn, G. Cremonese, S. Verani, and A. Zin, Meteor showers on the lunar atmosphere, *Earth Moon Planets*, **85**, 479-486, 2001.

[2] Bida T. A., R. M. Killen, T. H. Morgan, Discovery of calcium in Mercury's atmosphere, *Nature*, **404**, 159-161, 2000.

[3] Broadfoot, A. L., S. Kumar, M. J. S. Belton, and M. B. McElroy, Mercury's atmosphere from Mariner 10: Preliminary results, *Science*, **185**, 166 - 169, 1974.

[4] Broadfoot, A. L., D. E. Shemansky, and S. Kumar, Mariner 10: Mercury atmosphere, *Geophys. Res.* Lett., **3**, 577 - 580, 1976.

[5] Chase, S. C., Miner, E. D., Morrison, D., Much, G., and G. Neugebauer, Mariner 10 infrared radiometer result: Temperatures and thermal properties of the surface of Mercury, *Icarus*, **28**, 655-678, 1976.

[6] Cheng, A. F., R. E. Johnson, S. M. Krimigis, and L. Z. Lanzeroti, Magnetosphere, Exosphere, and Surface of Mercury, *Icarus*, **71**, 430 - 440, 1987.

[7] Cintala, M. Impact induced thermal effects in the lunar and Mercurian regoliths, J. *Geophys. Res.*, **97**, 947-973, 1992.

[8] Cremonese, G. and S. Verani, High resolution observations of the sodium emission from the Moon, *Adv. Space Res.*, **19**, 1561 - 1575, 1997.

[9] Delcourt, D. C., T. E. Moore, S. Orsini, A. Milillo, and J.-A. Sauvaud, Centrifugal acceleration of ions near Mercury, *Geophys. Res.* Lett., **29**, doi:10.1029/2001GL013829, 2002.

[10] Delcourt, D. C., S. Grimald, F. Leblanc, J. -J. Bertherlier, A. Millilo, and A. Mura, A quantitative model of planetary Na+ contribution to Mercury's magnetosphere, Ann. *Geophysicae*, **21**, 1723-1736, 2003.

[11] Flynn, B. and M. Mendillo, A picture of the Moon's atmosphere, *Science*, **261**, 184 - 186, 1993.

[12] Flynn, B. C. and S. A. Stern, A spectroscopic survey of metallic species abundances in the lunar atmosphere, *Icarus*, **124**, 530 - 536, 1996.

[13] Goldstein, B. D., S. T. Suess, and R. J. Walker, Mercury: Magnetospheric processes and the atmospheric supply and loss rate, *J. Geophys. Res.*, **86**, 5485 - 5499, 1981.

[14] Hapke, B., Space weathering from Mercury to the asteroid belts, *J. Geophys. Res.*, **106**, 10,039-10,074, 2001.

[15] Hale, A. S. and B. Hapke, A time-dependent model of radiative and conductive thermal energy transport in planetary regoliths with application to the Moon and Mercury, *Icarus*, **156**, 318-334, 2002.

[16] Hayakawa, H., Y. Kasaba, H. Yamakawa, H. Ogawa, and T. Mukai, The BepiColombo/MMO model payload and operation plan, *Adv. Space Res.*, **33**, 2142-2146, 2004.

[17] Hodges, R. R., J. H. Hoffman, and F. S. Johnson, The lunar atmosphere, *Icarus*, **21**, 415-426, 1974.

[18] Hunten, D. M., T. M. Morgan, and D. M. Shemansky, The Mercury atmosphere, p. 562-612 in MERCURY, eds. F. Vilas, C. Chapman, M. Matthews, U. of Arizona Press, Tucson, 1988.

[19] Hunten, D. M. and A. L. Sprague, Origin and Character of the Lunar and Mercurian Atmospheres, *Adv. Space Res.*, **19**, 1551-1560, 1997.

[20] Hunten, D. M., G. Cremonese, A. L. Sprague, R. E. Hill, S. Verani, and R. W. H. Kozlowski, The Leonid meteor shower and the lunar sodium atmosphere, *Icarus*, **136**, 298-303, 1998.

[21] Hunten D. M. and A. L. Sprague, Diurnal variation of Na and K at Mercury, *Meteor. and Planet. Sci.*, **37**, 1191-1195, 2002.

[22] Ip, W. -H., The sodium exosphere and magnetosphere of Mercury, *Geophys. Res. Lett.*, **13**, 423-426, 1986.

[23] Ip, W. -H., Mercury's magnetospheric irradiation effect on the surface, *Geophys. Res. Lett.*, **14**, 1191-1194, 1987.

[24] Ip, W. -H., On solar radiation-driven surface transport of sodium atoms at Mercury, *Astrophys. J.*, **356**, 675 - 681, 1990.

[25] Johnson, R. E., Energetic charged particle interactions with atmospheres and surfaces, Springer-Verlag, Berlin, 1990.

[26] Johnson, R. E. and R. Baragiola, Lunar surface: Sputtering and secondary ion mass spectroscopy, *Geophys. Res. Lett.*, **18**, 2169 - 2172, 1991.

[27] Johnson, R. E. and T. I. Quickenden, Photolysis and Radiolysis of Water Ice on Outer Solar System Bodies, *J. Geophys. Res.*, **102**, 10,985-10,996, 1997.

[28] Kabin, K., T. I. Gombosi, D. L. DeZeeuw, and K. G. Powell, Interaction of Mercury with the solar wind, *Icarus*, **143**, 397-406, 2000.

[29] Kallio, E. and P. Janhunen, Solar wind and magnetospheric ion impact on Mercury's surface, *Geophys. Res. Lett.*, **30**, 1877, 10.1029/2003GL017842, 2003.

[30] Killen, R. M. and W. -H. Ip, The surface-bounded atmospheres of Mercury and the Moon, *Rev. Geophys.*, **37**, 361-406, 1999.

[31] Killen, R. M., A. E. Potter, P. Reiff, M. Sarantos, B. V. Jackson, P. Hick, and B. Giles, Evidence for Space Weather at Mercury, *J. Geophys. Res.*, **106**, 20,509-20,525, 2001.

[32] Killen, R. M., M. Sarantos, A. E. Potter, and P. Reiff, Source rates and ion recycling rates for Na and K in Mercury's atmosphere, *Icarus*, **171**, 1-19, 2004.

[33] Kozlowski, R. W. H., A. L. Sprague, and D. M. Hunten, Observations of potassium in the tenuous lunar atmosphere, *Geophys. Res. Lett.*, **7**, 2253-2256, 1990.

[34] Leblanc, F. and R. E. Johnson, Mercury's sodium exosphere, *Icarus*, **164**, 261 - 281, 2003.

[35] Leblanc, F., J. G. Luhmann, R. E. Johnson, and M. Liu, Solar energetic particle event at Mercury, *Planet. Space Sci.*, **51**, 339-352, doi: 10.1016/S0032-0633(02)00207-6, 2003a.

[36] Leblanc F., D. Delcourt, and R. E. Johnson, Mercury's sodium exosphere: Magnetospheric ion recycling, *J. Geophys. Res.*, **108**, 5136, doi: 10.1029/2003JE002151, 2003b.

[37] Love, S. G. and D. E. Brownlee, A direct measurement of the terrestrial mass accretion rate of cosmic dust, *Science*, **262**, 550 - 553, 1993.

[38] Luhmann, J. G., C. T. Russell, and N. A. Tsyganenko, Disturbances in Mercury's magnetosphere: Are Mariner

10 "substorms" simply driven?, *J. Geophys Res.*, **103**, 9113-9119, 1998.

[39] Nash, D. B., D.L. Matson, T. V. Johnson, and F. P. Fanale, Na-D line emission from rock specimens by proton bombardment: Implications for emissions from Jupiter's satellite Io, *J. Geophys. Res.*, **80**, 1875-1879, 1975.

[40] Madey, T. E., B. V. Yakshinskiy, V. N. Ageev, and R. E. Johnson, Desorption of alkali atoms and ions from oxide surfaces: Relevance to origins of Na and K in atmospheres of Mercury and the Moon, *J. Geophys. Res.*, **103**, 5873 - 5887, 1998.

[41] Madey, T. E., R. E. Johnson, and T. M. Orlando, Far-out surface science: radiation-induced surface processes in the solar system, *Surf. Sci.*, **500**, 838-858, 2002.

[42] Massetti, S., S. Orsini, A. Milillo, A. Mura, E. de Angelis, H. Lammer, and P. Wurz, Mapping of the cusp plasma precipitation on the surface of Mercury, *Icarus*, **166**, 229-237, 2003.

[43] McGrath, M. A., R. E. Johnson, and L. J. Lanzerotti, Sputtering of sodium on the planet Mercury, *Nature*, **323**, 694-696, 1986.

[44] Mendillo, M., J. Baumgardner, and B. Flynn, Imaging observations of the extended sodium atmosphere of the Moon, *Geophys. Res. Lett.*, **18**, 2097-2100, 1991.

[45] Mendillo, M. and J. Baumgardner, Constraints on the origin of the Moon's atmosphere from observations during a lunar eclipse, *Nature*, **377**, 404 - 406, 1995.

[46] Mendillo, M., J. Baumgardner, and J. Wilson, Observational test for the solar wind sputtering origin of the Moon's extended sodium atmosphere, *Icarus*, **137**, 13 - 23, 1999.

[47] Misawa, H., A. Morioka, S. Okano, and K. Takamizawa, Investigations of distribution characteristics of Mercury's atmosphere: Studies based on a model calculation and ground-based observation, *Proc. 35th ISAS Lunar Planet.* Symp., 199-203, 2002a.

[48] Misawa, H., I. Yoshikawa, T. Takashima, R. Honda, Y. Uchihori, H. Kitamura, and N. Takeyama, Radiation tests of optical lasses for BepiColombo/MMO imaging camera, *ISAS report* **120**, 1 - 10, 2002b.

[49] Morgan, T. H., H. A. Zook, and A. E. Potter, Impact-driven supply of sodium and potassium to the atmosphere of Mercury, *Icarus*, **75**, 156-170, 1988.

[50] Morgan, T. H., H. A. Zook, and A. E. Potter, Production of sodium vapor from exposed regolith in the inner solar system, *Proc. Lunar Plan. Sci. Conf.*, **19**, 297 - 304, 1989.

[51] O'Keefe, J. D. and T. J. Ahrens, Impact induced energy partitioning, melting, and vaporization on terrestrial planets, *Lunar Planet. Sci.*, **8**, 3357-3374, 1977.

[52] Pierazzo, E. and H. J. Melosh, Hydrocode modeling of Chicxulub as an oblique impact event, *Earth Planet. Sci. Lett.*, **165**, 163-176, 1999.

[53] Potter, A. E. and T. H. Morgan, Discovery of sodium in the atmosphere of Mercury, *Science*, **229**, 651 - 653, 1985.

[54] Potter, A. E. and T. H. Morgan, Potassium in the atmosphere of Mercury, *Icarus*, **67**, 336 - 340, 1986.

[55] Potter, A. E. and T. H. Morgan, Variation of sodium on Mercury with solar radiation pressure, *Icarus*, **71**, 472 - 477, 1987.

[56] Potter, A. E. and T. H. Morgan, Discovery of sodium and potassium vapor in the atmosphere of the Moon, *Science*, **241**, 675 - 680, 1988.

[57] Potter, A. E. and T. H. Morgan, Evidence for magnetospheric effects on the sodium atmosphere of Mercury, *Science*, **248**, 835-838, 1990.

[59] Potter, A. E., Chemical sputtering could produce sodium vapor and ice on Mercury, *Geophys. Res. Lett.*, **22**,

3289 - 3292, 1995.

[60] Potter, A. E. and T. H. Morgan, Sodium and potassium atmospheres of Mercury, *Planet. Space Sci.*, **45**, 95 - 100, 1997a.

[61] Potter, A. E. and T. H. Morgan, Evidence for Suprathermal Sodium on Mercury, *Adv. Space Res.*, **19**, 1571 - 1576, 1997b.

[62] Potter, A. E., T. H. Morgan, and R. M. Killen, Rapid changes in the sodium exosphere of Mercury, *Planet. Space Sci.*, **47**, 1441-1448, 1999.

[63] Potter, A. E., C. M. Anderson, R. M. Killen, and T. H. Morgan, Ratio of sodium to potassium in the Mercury exosphere, *J. Geophys. Res.*, **107**, 10.1029/2000JE001493, 2002a.

[64] Potter, A. E., R. M. Killen, and T. H. Morgan, The sodium tail of Mercury, *Meteor. Planet. Science*, **37**, 1165-1172, 2002b.

[65] Potter, A. E., C. Plymate, C. Keller, and R. M. Killen, *American Astronomical Society Meeting* 204, #64.07, 2004.

[66] Roth, J., Chemical Sputtering, *in Sputtering by Particle Bombardment II, Gehrisch, R. Ed., Topics in Applied Physics*, **52**, Springer-Verlag, 91-145, 1983

[67] Sarantos, M., P. H. Reiff, T. W. Hill, R. M. Killen, and A. L. Urquhart, A Bx-interconnected magnetosphere model for Mercury, *Planet. Space Sci.*, **49**, 1629-1635, 2001.

[68] Slade, M. A., B. J. Butler, and D. O. Muhleman, Mercury radar imaging: Evidence for polar ice, *Science*, **258**, 635-640, 1992.

[69] Smith, S. M., J. K. Wilson, J. Baumgardner, and Mendillo, Discovery of the Distant Lunar sodium Tail and its Enhancement Following the Leonid Meteor Shower of 1998, *Geophys. Res. Lett.*, **26**, 1642 - 1652, 1999.

[70] Smyth, W. H., Nature and variability of Mercury's sodium atmosphere, *Nature*, **323**, 696-699, 1986.

[71] Smyth, W. H. and M. L. Marconi, Theoretical overview and modeling of the sodium and potassium atmospheres of Mercury, *Astrophys. J.*, **441**, 839-864, 1995.

[72] Sprague, A. L., R. W. H. Kozlowski, and D. M. Hunten, Caloris Basin: An enhanced source for potassium in Mercury's atmosphere, *Science*, **249**, 1140 - 1143, 1990.

[73] Sprague, A. L., Mercury's atmospheric bright spots and Potassium variations: A possible cause, *J. Geophys. Res.*, **97**, 18,257-18,269, 1992a.

[74] Sprague, A. L., A correction to Mercury's atmospheric sodium bright spots and potassium variations: A possible cause, *J. Geophys. Res.*, **98**, 1231, 1992b.

[75] Sprague, A. L., R. W. H. Kozlowski, D. M. Hunten, N. M. Schneider, D. L. Domingue, W. K. Wells, W. Schmitt, and U. Fink, Distribution and Abundance of Sodium in Mercury's Atmosphere, 1985 - 1988, *Icarus*, **129**, 506 - 527, 1997.

[76] Sprague, A. L., W. J. Schmitt, and R. E. Hill, Mercury: Sodium Atmospheric Enhancements, Radar Bright Spots and Visible Surface Features, *Icarus*, **135**, 60-68, 1998a.

[77] Sprague, A. L., D. M. Hunten, R. W. Kozlowski, F. A. Grosse, R. E. Hill, and R. L. Morris, Observations of sodium in the lunar atmosphere during international lunar atmosphere week, 1995, *Icarus*, **131**, 372 - 381, 1998b.

[78] Stern, S. A. and B. C. Flynn, Narrow-field imaging of the lunar sodium exosphere, *Astron. J.*, **109**, 835 - 841, 1995.

[79] Strom, R. G. and A. L. Sprague, Exploring Mercury, The iron Planet, Springer-Verlag Berlin, 2003.

[80] Sugita, S., Schultz P. H., and M. A. Adams, Spectroscopic measurements of vapor clouds due to oblique

impact, *J. Geophys. Res.*, **103**, 19,427-19,441, 1998.

[81] Takamizawa, K., Distribution of Herman Sodium Atmosphere, Master Thesis, Tohoku Univ., 2000.

[82] Takamizawa, K., H. Misawa, A. Morioka, and S. Okano, Model calculation of neutral sodium atmosphere of Mercury, Proc. 33rd ISAS Lunar Planet Symp., 149-152, 2000.

[83] Tyler, A. L., R. W. H. Kozlowski, and D.M. Hunten, Observations of sodium in the tenuous lunar atmosphere, *Geophys. Res. Lett.*, **15**, 1141 - 1144, 1988.

[84] Verani, S., C. Barbieri, C. R. Benn, G. Cremonese, and M. Mendillo, The 1999 Quadrantids and the lunar Na atmosphere, MNRAS, **327**, 244-248, 2001.

[85] Wiens, R. C., D. S. Burnett, W. F. Calaway, C. S. Hansen, K. R. Lykke, and M. J. Pellin, puttering Products of Sodium Sulfate: Implications for Io's Surface and for Sodium-Bearing Molecules in the Io Torus, *Icarus*, **128**, 386-397, 1997.

[86] Wilson, J. K., S. M. Smith, J. Baumgardner, and Mendillo, M., Modeling an Enhancement of the lunar sodium atmosphere and tail during the Leonid meteor shower of 1998, *Geophys. Res. Lett.*, **26**, 1649-1652, 1999.

[87] Wilson J. K., J. Baumgardner, and Mendillo, M. The outer limits of the lunar sodium exosphere, *Geophys. Res. Lett.*, **30**, 51-1, 1649, DOI 10.1029/2003GL017443, 2003.

[88] Yakshinskiy, B. V. and T. E. Madey, Photon-stimulated desorption as a substantial source of sodium in the lunar atmosphere, *Nature*, **400**, 642-644, 1999.

[89] Yakshinskiy, B. V., T. E. Madey, and V. N. Ageev, Desorption Induced by Electronic Transition of Na from SiO2: relevance to tenuous planetary atmospheres, *Surf. Sci.*, **451**, 160-165, 2000.

[90] Yakshinskiy, B. V. and T. E. Madey, Electron and photon-stimulated desorption of K from an ice surface. *J. Geophys.Res.*, **106**, 33303-33308, 2001.

[91] Yamakawa, H., H. Ogawa, Y. Kasaba, H. Hayakawa, T. Mukai, and M. Adachi, Current status of the BepiColombo/MMO spacecraft design, *Adv. Space Res.*, **33**, 2133-2141, 2004.

Appendix 1 : Instrument Data Sheet

Table A1: Performance of MSASI

Bandpass	589.1303-589.1863nm
Spectral resolution	0.007 nm
Spatial resolution	0.17°, corresponding to 1/64 R_M (~40 km) from 10,000km altitude.
Nominal sensitivity	20kR - 10 MR
Field of view	2° × 2 ° (× Spin scan and Mirror scan : 30° square)
Pointing	1 degree-of-freedom scanning system (scan range: 15°, spatial coverage 30°)
Observation types	Spectral imaging of Mercury's sodium exosphere
Telescope	Refractive optics with scanning mirror
Spectrometer type	Tandem Fabry-Perot Interferometer
Detector type	Image Intensifier with CMOS/APS
Photocathode	GaAsP
External dimensions	Main body : 60 (H) × 70 (V) × 330 (L) mm Scanning system : 100 (H) × 125 (V) × 110 (L) mm Entrance Hood : 50 (H) × 72 (V) × 150 (L) mm (Baseline)
Mass/ power	3.5 kg/ 12.2 W (maximum)
Operating Temperature	-10° C to +50° C
Typical Data Volume	Normal mode 3.2Mbyte/orbit High priority mode 9.6Mbyte/orbit (e.g. True Anomaly Angle is 60°.) Low priority mode 1.6Mbyte/orbit (e.g. True Anomaly Angle is 180°.)

Appendix 2 : Development and Verification

1 Baseline Schedule

The MSASI baseline schedule is summarized in **figure.**

(FY: Fiscal year from April to March in Japan.)

[2004FY]

1Q/2005 **MMO Instrument Preliminary Requirements Review (MMO-I-PRR)**

Requirement to the system will be fixed.

Development/test of each BBM component will start.

Mechanical Design: Selection of key parts (motor, gear, hood, etc.)

Mechanical test by BBM

Thermal Design: Development of TMM

Electronics Design: Close of Conceptual design

Gearing control/analysis: Start of Conceptual design

[2005FY]

Request to JAXA/ESA: **Fix of Mechanical Environment Condition at 2Q/2005**

BBM: Development
Test by "10-solar simulator" [TBD] (key element, hood/BBM)
EM: Design Start from First half (equivalent to EQM)
STM: Design Start from Second half
Software: Close of Conceptual design

[2006FY]

2Q/2006 **MMO Instrument Preliminary Design Review (MMO-I-PDR)**
STM/EM design will be fixed.
Development of each STM/EM component will start.
EM: Development (MSASI-E, MSASI-G, MSASI-M)
STM: Development (MSASI-H), thermal dummy (MSASI-E, -G, -M)
Extension control/analysis: Start of Conceptual design
Software: Development

[2007FY]

2 or 3Q/2007 Delivery of MSASI STM to JAXA
- AIV of MMO-STM will start.

AIV of MSASI-EM will start.

4Q/2007 **Delivery of MSASI EM/EGSE to JAXA**
- AIV of PCS-MSASI will start at JAXA
- Instrumental EMC Test for all subsystems (if required)

1Q/2008 **MMO Instrument Critical Design Review (MMO-I-CDR)**
FM design will be fixed.
Development of each FM components will start.
EM: MSASI-G, MSASI-E, MSASI-M tests
STM: MMO-STM test
Software: PCS Software test
FM: Design Start

[2008FY]

4Q/2008 **Delivery of each FM/EGSE component to ISAS/JAXA.**
- AIV of MSASI-FM will start at ISAS/JAXA.

1Q/2009 **Delivery of MSASI FM/EGSE to JAXA.**
- AIV of PCS-MSASI will start at JAXA.
FM: Development
MSASI FM Test >> PCS FM Test

[2009FY]

2Q/2009 **Delivery of MSASI FM/EGSE to JAXA**
- First Integration and Test of MMO

3Q/2009 **Return of the MSASII to the team**
- Instrumental Environment Test

1Q/2010	**Final Delivery of MSASI FM/EGSE to JAXA**
	MMO Instrument Qualification Review (MMO-I-QR)
	- AIV of MMO-FM will start.
FM:	MMO First Integration Test @ ISAS/JAXA
	>> Environment Test >> MMO AIV start @ ISAS/JAXA
[2010FY]	
4Q/2010	**MMO Qualification Review (MMO-QR)**
	- Shipment of MMO to ESTEC
	- AIV of the MCS FM will start at ESTEC.
FM:	MMO AIV @ ISAS/JAXA >> MCS AIV @ ESTEC
[2011FY]	
4Q/2011	**MCS Flight Acceptance Review (MCS-FAR)**
	- Shipment of MCS to the Launch Site
FM:	MCS AIV @ ESTEC >> Transport to Launch site
[2012FY]	
2Q/2012	Launch

JAXA Research and Development Report
(JAXA-RR-05-007E)

Date of Issue : Nobember 30, 2005

Edited and Published by :
Japan Aerospace Exploration Agency
2-1-1 Sengen, Tsukuba-shi,
Ibaraki 305-8508 Japan

Printed by :
WORK1 Co., Ltd.
1-14-2 Tanashioda, Sagamihara-shi, Kanagawa 229-1125 Japan

Japan Aerospace Exploration Agency